

Isogeometric Bézier dual mortaring: the Kirchhoff-Love shell problem

Di Miao¹, Zhihui Zou ^{*2,3}, Michael A. Scott^{1,3}, Michael J. Borden³, and Derek C. Thomas³

¹Department of Civil and Environmental Engineering, Brigham Young University, Provo, UT USA

²Oden Institute for Computational Engineering and Sciences, The University of Texas at Austin, Austin, TX USA

³Coreform LLC, Orem, UT USA

April 13, 2021

Abstract

In this paper we develop an isogeometric Bézier dual mortar method for coupling multi-patch Kirchhoff-Love shell structures. The proposed approach weakly enforces the continuity of the solution at patch interfaces through a dual mortar method and can be applied to both conforming and non-conforming discretizations. As the employed dual basis functions have local supports and satisfy the biorthogonality property, the resulting stiffness matrix is sparse. In addition, the coupling accuracy is optimal because the dual basis possesses the polynomial reproduction property. We also formulate the continuity constraints through the Rodrigues' rotation operator which gives a unified framework for coupling patches that are intersected with G^1 continuity as well as patches that meet at a kink. Several linear and nonlinear examples demonstrated the performance and robustness of the proposed coupling techniques.

1 Introduction

Thin-walled structures are widely used in nature and technology due to their optimal load-carrying capacity. With the dimension in thickness direction being significantly smaller than those in other directions, thin-walled structures can be readily described by a surface and a director vector field associated with it. This geometrical reduction from volume to surface not only largely simplifies the meshing process of finite element analysis (FEA) but also significantly reduces the analysis cost because shell elements based on surface meshes can be used and they are usually more efficient than solid elements for thin-walled structures. Among various shell formulations, the Reissner-Mindlin [1, 2, 3, 4, 5, 6, 7] and the Kirchhoff-Love [3, 8, 9, 7] theories are the most widely used. Kirchhoff-Love shells are attractive because they require fewer degrees of freedom per node and do not suffer from shear locking found in Reissner-Mindlin shell elements [10, 11, 12, 13]. However, Kirchhoff-Love shell theory requires C^1 -continuity constraints across element interfaces, which cannot be easily satisfied by traditional FEA based on C^0 -continuous Lagrange polynomials. In contrast, Reissner-Mindlin shell theory only requires C^0 -continuity, therefore dominating current commercial FEA software.

Over the past decade, isogeometric analysis (IGA) [14] which adopts the CAD description as the basis for analysis, has emerged as one of the hottest research topics in computational mechanics. Superior performance of IGA has been demonstrated in various fields, such as structural mechanics [15, 16, 17], optimization [18, 19], electromagnetics [20, 21] and fluid-structure interaction [22, 23], etc. Since most CAD packages make use of boundary or surface representations to model geometrical objects and shell analysis does not require volumetric description of the underlying geometry, IGA has become an ideal tool for shell analysis. Additionally, CAD technologies like Non-Uniform Rational B-Splines (NURBS) [24] and T-splines [25] make it easier to define higher-order continuous basis for analysis, which opens the door to new shell formulations based on both Reissner-Mindlin and Kirchhoff-Love shell theories [26, 1, 27, 28, 29, 30, 31, 32]. This is particularly true for Kirchhoff-Love shells due to the intrinsic C^1 -continuity requirement.

*Corresponding author: zhihuzou1988@gmail.com

Even though it is convenient to achieve a higher-order continuous spline basis in the patch interior, complex shell structures are usually modeled by multiple patches and the basis functions along patch interfaces are usually discontinuous. Additionally, adjacent patches often have non-conforming control point layouts, different parameterizations and even gaps along the interfaces. These non-conforming discretizations are usually not an issue from a design perspective but appropriate continuity constraints have to be applied to achieve the well-posedness of the underlying finite element analysis. For Reissner-Mindlin shells, only C^0 -continuity constraints are required along patch interfaces. However, for Kirchhoff-Love shells, more challenging C^1 -continuity constraints are necessary to transfer bending moments across G^1 -continuous patch interfaces. Also, if a kink occurs at a patch interface, the angle of the kink has to be preserved to prevent the hinge-like effect at the joint [33, 34].

1.1 Key contributions

In this paper, we propose a dual mortar method for coupling multi-patch Kirchhoff-Love shells. This approach is capable of coupling both conforming and non-conforming multi-patch Kirchhoff-Love shell structures and can be applied to either linear or nonlinear problems. This dual mortar method utilizes the enriched dual basis [35] which leads to the following properties:

- The Lagrange multipliers used to apply the continuity constraints can be easily condensed out and the resulting stiffness matrix is sparse. This property is ensured by the fact that the enriched dual basis is local and satisfies the biorthogonality property [36, 37, 35].
- Optimal coupling accuracy is achieved as the enriched dual basis possesses the polynomial reproduction property [38, 35].
- A particular solution of the non-homogeneous constraint equations can be explicitly constructed based on the enriched dual basis without any additional computational cost. In this way, the system of equations with nonlinear constraints, introduced by the kinks between patches, can be solved more efficiently.

Additionally, we also devise a new continuity constraint formulation based on the Rodrigues' rotation operator. This rotation operator is defined by the coupling angle between adjacent patches, which gives a general framework for coupling multi-patch Kirchhoff-Love shells with smooth interfaces or kinks.

1.2 Prior work

In recent years a large amount of research effort has been devoted to simulating multi-patch thin-walled structures as Kirchhoff-Love shells. The primal focus has been dedicated to devising robust techniques to apply the continuity constraints between patches. Kiendl et al. [8] proposed the so-called bending strip method to couple multi-patch Kirchhoff-Love shells with conforming discretizations along interfaces. This method approximately applies continuity constraints by adding fictitious bending stiffness. Because the magnitude of the fictitious stiffness is determined by a penalty-like parameter, this method can be considered to be a penalty method. While penalty method is usually easy to implement, the performance can be significantly influenced by the choice of penalty parameters. More specifically, a small penalty parameter cannot effectively enforce the constraints while a large penalty can lead to an ill-conditioned system. Inspired by the connection between the penalty method and the stiff mechanical system, Goyal and Simeon [34] improved the condition number of the bending strip method by removing the penalty parameter dependence. To handle non-conforming meshes, Herrema et al. [39] proposed a penalty formulation that weakly imposes the continuity constraints on both displacement and rotation terms, and this formulation requires only one dimensionless penalty coefficient. In addition to coupling patches that intersect with each other along patch boundaries, penalty methods have also been used for coupling trimmed Kirchhoff-Love patches [40].

Apostolatos et al. [41] introduced the Lagrange multiplier method to couple multi-patch Kirchhoff-Love shells with non-conforming meshes. Duong et al. [32] proposed a new formulation of continuity constraints for Kirchhoff-Love shells and applied the constraints with both penalty and Lagrange multiplier methods on conforming meshes. Recently, Hirschler et al. [42] developed a formulation based on the Lagrange multiplier method to impose the continuity constraints between non-conforming patches and applied it to shape optimization of stiffened multi-patch structures. Unlike penalty methods, Lagrange multiplier methods do not introduce problem-dependent parameters but they lead to a saddle point problem which usually has *inf-sup* instability unless the Lagrange multiplier space is carefully constructed.

Schuß et al. [43] condensed out the Lagrange multipliers by embedding the continuity constraints into the basis. In this way, the problem becomes positive definite but the resulting stiffness matrix is usually fully populated.

Another popular method used for coupling Kirchhoff-Love shells is the Nitsche's method [44, 45, 46]. The advantage of Nitsche's method is that it neither has instability issues nor introduces additional degrees-of-freedom like Lagrange multipliers. However, to achieve analysis accuracy, the stability parameters need to be obtained through solving eigenvalue problems on elements along patch interfaces. Additionally, for nonlinear problems the implementation of Nitsche's method becomes complex as it requires calculating the variations of the traction. Besides the aforementioned multi-patch coupling methods which are most closely related to the proposed approach, there are plenty of works that directly apply continuity constraints on element boundaries based on other CAD techniques, such as the subdivision surfaces [47, 9, 48] and the rational triangular Bézier splines techniques [49, 50], etc.

This paper is organized as follows: Section 2 briefly reviews the fundamentals of the B-spline basis and its dual bases, followed by an introduction of the general framework of the dual mortar method. Section 3 describes the basic kinematic assumptions and the variational form of Kirchhoff-Love shells. We then present the details of the proposed coupling approach in Section 4. Several linear and nonlinear benchmark problems are given in Section 5 to demonstrate the performance of the presented method. Conclusions are drawn in Section 6.

2 Preliminary

2.1 Spline fundamentals

2.1.1 B-spline basis

A univariate B-spline basis is defined by a knot vector $\Xi = \{\xi_1, \xi_2, \dots, \xi_{n+p+1}\}$, which consists of a non-decreasing sequence of real numbers, $\xi_i \leq \xi_{i+1}, i = 1, \dots, n+p+1$, where p is the degree of the B-spline basis functions and n is the number of basis functions. The i th B-spline basis function of degree p , denoted by $N_{i,p}(\xi)$, can be recursively defined by

$$N_i^0(\xi) = \begin{cases} 1 & \xi_i \leq \xi \leq \xi_{i+1} \\ 0 & \text{otherwise} \end{cases}, \quad (1)$$

$$N_i^p(\xi) = \frac{\xi - \xi_i}{\xi_{i+p} - \xi_i} N_i^{p-1}(\xi) + \frac{\xi_{i+p+1} - \xi}{\xi_{i+p+1} - \xi_{i+1}} N_{i+1}^{p-1}(\xi), \quad (2)$$

A Non-uniform rational B-spline basis function is defined as

$$R_i^p(\xi) = \frac{N_i^p(\xi) w_i}{W(\xi)} \quad (3)$$

where the positive number w_i is the weight corresponding to basis function N_i^p and the denominator $W(\xi)$ is called the weighting function given as

$$W(\xi) = \sum_j N_j^p(\xi) w_j. \quad (4)$$

Note that the superscript p will be omitted hereafter for conciseness.

2.1.2 Dual basis

For a B-spline basis $\{N_i\}_{i=1}^n$, a dual basis $\{\hat{N}_i\}_{i=1}^n$ satisfies the biorthogonality relation:

$$\langle \hat{N}_i, N_j \rangle_{\Omega} := \int_{\Omega} \hat{N}_i N_j d\Omega = \delta_{ij}, \quad i, j \in \{1, 2, \dots, n\}, \quad (5)$$

where δ_{ij} denotes the Kronecker delta. The global dual basis functions $\{\hat{N}_i^G\}_{i=1}^n$ are defined as:

$$\hat{N}_i^G = \sum_j G_{ij}^{-1} N_j, \quad (6)$$

where G_{ij}^{-1} are the components of the inverse of the Gramian matrix \mathbf{G} with components $G_{ij} = \langle N_i, N_j \rangle_{\Omega}$. One limitation of the global dual basis functions is that they do not preserve compact support and will result in dense linear systems when used to discretize Lagrange multipliers.

To maintain the sparsity of the stiffness matrix while keep the optimal convergence, the enriched Bézier dual basis functions introduced in [35] will be utilized in this work. The enriched Bézier dual basis functions possess the following properties:

- Local support
- Easy construction
- Reproduction of higher-order polynomials

The enriched Bézier dual basis functions have demonstrated excellent convergence performance for both second order and fourth order problems [35]. A comparison of the support sizes of a global dual basis function and different enriched Bézier dual basis functions is given in Figure 1. As can be seen, for the primal cubic B-spline basis function shown in Figure 1a, its global dual basis in Figure 1b has a global support while its enriched Bézier dual basis functions with different orders of polynomial reproduction property have compact supports as shown in Figures 1c to 1f. Note that the enriched dual basis function in Figure 1c is identical to the Bézier dual basis functions proposed in [36] because it only has the ability to produce constants. For simplicities, we omit the details about constructing the enriched dual basis here. Readers are referred to [35] for a detailed description of the algorithm.

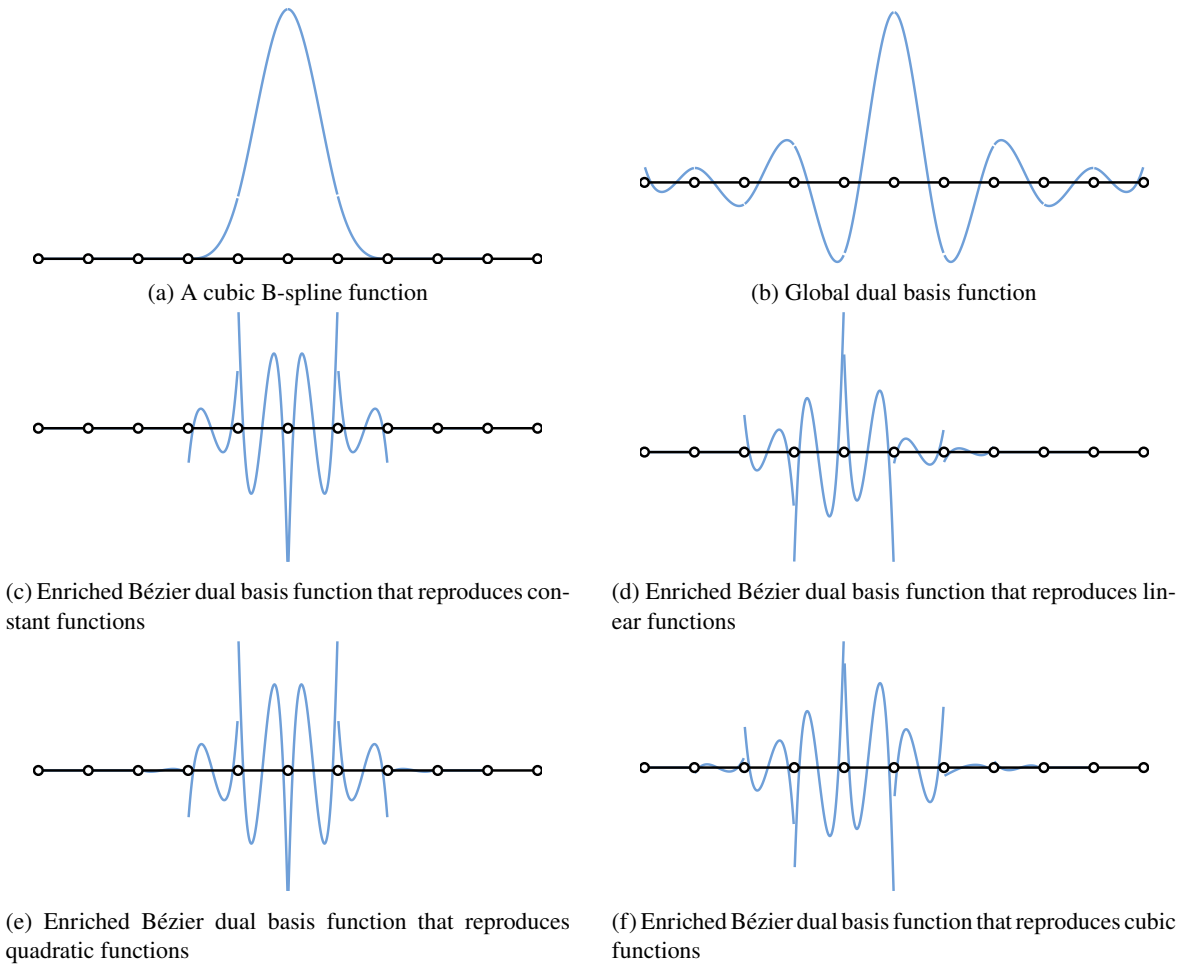


Figure 1: A cubic B-spline basis function, its corresponding global dual basis function and enriched Bézier dual basis functions with different polynomial reproduction orders.

2.2 Dual mortar method

In this section, we briefly recall the dual mortar method in the context of an abstract formulation for a constrained problem: find $u \in \mathcal{X}$ and a Lagrange multiplier $\lambda \in \mathcal{M}$ such that

$$\begin{cases} a(v, u) + b(v, \lambda) = l(v) & \forall v \in \mathcal{X}, \\ b(\mu, u) = c(\mu) & \forall \mu \in \mathcal{M}, \end{cases} \quad (7a)$$

where \mathcal{X} is a Hilbert space that satisfies homogeneous Dirichlet boundary condition on $\partial\Omega$, \mathcal{M} is an appropriate Lagrange multiplier space, $a(\cdot, \cdot)$ is a bilinear form representing a potential energy, $l(\cdot)$ is a linear form representing the external load, $b(\cdot, \cdot)$ and $c(\cdot)$ are the bilinear and linear forms representing a set of constraints on the solution u , and v and μ are testing functions for the solution u and the Lagrange multiplier λ , respectively. In Section 4, $b(\cdot, \cdot)$ and $c(\cdot)$ will represent the non-homogeneous continuity constraints across patch boundaries for each Newton-Raphson iteration.

If we introduce a pair of discrete function spaces $\mathcal{X}^h \subset \mathcal{X}$ and $\mathcal{M}^h \subset \mathcal{M}$, the weak form (7) can be discretized into the following linear problem

$$\mathbf{K}^{\text{LM}} \mathbf{U}^{\text{LM}} = \begin{bmatrix} \mathbf{K} & \mathbf{B}^T \\ \mathbf{B} & \mathbf{0} \end{bmatrix} \begin{bmatrix} \mathbf{U} \\ \mathbf{\Lambda} \end{bmatrix} = \begin{bmatrix} \mathbf{F} \\ \mathbf{R} \end{bmatrix}, \quad (8)$$

where \mathbf{K} is the discretized stiffness matrix, \mathbf{F} is the discretized external force vector, \mathbf{B} is the discretized constraints matrix, \mathbf{R} is the forcing term due to non-homogeneous constraints (for homogeneous constraints, $\mathbf{R} = \mathbf{0}$), and \mathbf{U} and $\mathbf{\Lambda}$ are the vectors of displacement and Lagrange multiplier variables, respectively. The dual mortar method statically condenses out additional unknowns and gives rise to a positive definite variational problem defined on a constrained function space as

$$\mathcal{V}^h := \{u^h \in \mathcal{X}^h \mid b(\lambda^h, u^h) = 0, \quad \forall \lambda^h \in \mathcal{M}^h\}. \quad (9)$$

The saddle point problem (7) can now be transformed into a minimization problem: find a general solution $u_{\text{hom}}^h \in \mathcal{V}^h$ such that, for $u^h = u_{\text{hom}}^h + u_{\text{non}}^h$,

$$a(v^h, u^h) = l(v^h), \quad \forall v^h \in \mathcal{V}^h, \quad (10)$$

where $u_{\text{non}}^h \in \mathcal{X}^h$ is a particular solution that satisfies the constraint (7b). Given, $\mathbf{N}^{\mathcal{X}^h}$, a vector containing the basis functions of \mathcal{X}^h , the vector containing the basis functions of \mathcal{V}^h is given by

$$\mathbf{N}^{\mathcal{V}^h} = [\mathbf{B}^\perp]^T \mathbf{N}^{\mathcal{X}^h}, \quad (11)$$

where all column vectors of \mathbf{B}^\perp are linearly independent and they span the null space of \mathbf{B} . We can further partition \mathbf{U} as

$$\mathbf{U} = \begin{bmatrix} \mathbf{U}_s \\ \mathbf{U}_m \\ \mathbf{U}_{\text{in}} \end{bmatrix}, \quad (12)$$

where the slave nodal displacement vector \mathbf{U}_s consists of all degrees of freedom involved in the constraint that will be eliminated after the static condensation, the master nodal displacement vector \mathbf{U}_m consists of all degrees of freedom involved in the constraint that will be kept after the static condensation, and the inactive nodal vector \mathbf{U}_{in} consists of all degrees of freedom that do not contribute to the construction of \mathbf{B} . The constraint can then be rewritten as

$$\mathbf{B}\mathbf{U} = \begin{bmatrix} \mathbf{B}_s & \mathbf{B}_m & \mathbf{0} \end{bmatrix} \begin{bmatrix} \mathbf{U}_s \\ \mathbf{U}_m \\ \mathbf{U}_{\text{in}} \end{bmatrix} = \mathbf{0}. \quad (13)$$

If the Lagrange multiplier space is discretized with dual basis functions and the continuity constraint is dual compatible, \mathbf{B}_s is the identity matrix, and the bandwidth of \mathbf{B}_m depends on the support size of the dual basis functions. For a constraint matrix \mathbf{B} , constructed with dual basis functions with compact support, \mathbf{B}_m is a sparse matrix with limited bandwidth, while global dual basis functions lead to a dense \mathbf{B}_m . For a \mathbf{B} that takes the form (13) with $\mathbf{B}_s = \mathbf{I}$, the corresponding \mathbf{B}^\perp can be obtained from

$$\mathbf{B}^\perp = \begin{bmatrix} -\mathbf{B}_m & \mathbf{0} \\ \mathbf{I} & \end{bmatrix}. \quad (14)$$

For any full column rank matrix \mathbf{B} , a particular solution can be solved by taking the Moore-Penrose inverse [51] as

$$\mathbf{U}^{\text{non}} = \mathbf{B}^T [\mathbf{B}\mathbf{B}^T]^{-1} \mathbf{R}. \quad (15)$$

If $\mathbf{B}_s = \mathbf{I}$, a particular solution of a constraint matrix that takes the form (13) can be explicitly constructed as

$$\mathbf{U}^{\text{non}} = \begin{bmatrix} \mathbf{R} \\ \mathbf{0} \end{bmatrix}. \quad (16)$$

The substitution of the constrained basis functions (11) into the mortar formulation (10) leads to the following linear system:

$$\mathbf{K}^{\text{mortar}} \mathbf{U}^{\text{mortar}} = [\mathbf{B}^\perp]^T \mathbf{K} \mathbf{B}^\perp \mathbf{U}^{\text{mortar}} = [\mathbf{B}^\perp]^T \mathbf{F} - [\mathbf{B}^\perp]^T \mathbf{K} \mathbf{U}^{\text{non}}. \quad (17)$$

The relation between the mortar displacement nodal value vector $\mathbf{U}^{\text{mortar}}$ and the homogeneous solution \mathbf{U}^{hom} is given by

$$\mathbf{U}^{\text{hom}} = \mathbf{B}^\perp \mathbf{U}^{\text{mortar}}. \quad (18)$$

The displacement nodal value vector of the original saddle point problem can be written as

$$\mathbf{U} = \mathbf{U}^{\text{hom}} + \mathbf{U}^{\text{non}}. \quad (19)$$

With a sparse \mathbf{B}^\perp obtained from a set of dual basis functions with compact supports, the stiffness matrix of the mortar formulation $\mathbf{K}^{\text{mortar}}$ will remain sparse, resulting in an efficient linear system.

3 Formulation of Kirchhoff-Love shell

In this section, we present the formulation of Kirchhoff-Love shell in compact form. A thorough study of finite element shell modeling can be found in [3]. The Kirchhoff-Love shell theory assumes that the normal of the midsurface remains perpendicular to midsurface in the deformed configuration. Hence, the transverse strains are zero and the description of shell geometry can be reduced to its midsurface.

3.1 Kinematics

As shown in Figure 2, the reference and current configurations, \mathbf{X} and \mathbf{x} , of a three-dimensional shell body can be parameterized as

$$\begin{cases} \mathbf{X}(\theta^1, \theta^2, \theta^3) = \mathbf{R}(\theta^1, \theta^2) + \theta^3 \mathbf{A}_3(\theta^1, \theta^2) \\ \mathbf{x}(\theta^1, \theta^2, \theta^3) = \mathbf{r}(\theta^1, \theta^2) + \theta^3 \mathbf{a}_3(\theta^1, \theta^2) \end{cases}, \quad (20)$$

where \mathbf{R} and \mathbf{r} are the midsurfaces, \mathbf{A}_3 and \mathbf{a}_3 are the unit director vectors of \mathbf{R} and \mathbf{r} , respectively, θ^1 and θ^2 denote the curvilinear coordinates, and $-\frac{h}{2} \leq \theta^3 \leq \frac{h}{2}$, where h is the thickness of the shell. We assume, without loss of generality, that $0 \leq \theta^1, \theta^2 \leq 1$. The Kirchhoff-Love shell theory assumes that the director vector remains perpendicular to the midsurface in the deformed configuration. Therefore, \mathbf{A}_3 and \mathbf{a}_3 are defined similarly as

$$\begin{cases} \mathbf{A}_3 = \frac{\mathbf{A}_1 \times \mathbf{A}_2}{|\mathbf{A}_1 \times \mathbf{A}_2|} \\ \mathbf{A}_\alpha = \mathbf{R}_{,\alpha} = \frac{\partial \mathbf{R}}{\partial \theta^\alpha} \end{cases} \quad \text{and} \quad \begin{cases} \mathbf{a}_3 = \frac{\mathbf{a}_1 \times \mathbf{a}_2}{|\mathbf{a}_1 \times \mathbf{a}_2|} \\ \mathbf{a}_\alpha = \mathbf{r}_{,\alpha} = \frac{\partial \mathbf{r}}{\partial \theta^\alpha} = \mathbf{A}_\alpha + \mathbf{u}_{,\alpha} \end{cases}, \quad (21)$$

where \mathbf{A}_α and \mathbf{a}_α are the tangent vectors of the midsurfaces in the reference and current configurations, and $|\cdot|$ denotes the Euclidean length of the given vector. Note that we adopt the established convention for Latin and Greek indices (i.e., $i = 1, 2, 3$ and $\alpha = 1, 2$) here and henceforth. The midsurface displacement field is defined as

$$\mathbf{u}(\theta^1, \theta^2) = \mathbf{r}(\theta^1, \theta^2) - \mathbf{R}(\theta^1, \theta^2). \quad (22)$$

The covariant base vectors at an arbitrary material point of the reference and current configurations are defined respectively as

$$\begin{cases} \mathbf{G}_\alpha = \mathbf{X}_{,\alpha} = \mathbf{A}_\alpha + \theta^3 \mathbf{A}_{3,\alpha} \\ \mathbf{G}_3 = \mathbf{X}_{,3} = \mathbf{A}_3 \end{cases} \quad \text{and} \quad \begin{cases} \mathbf{g}_\alpha = \mathbf{x}_{,\alpha} = \mathbf{a}_\alpha + \theta^3 \mathbf{a}_{3,\alpha} \\ \mathbf{g}_3 = \mathbf{x}_{,3} = \mathbf{a}_3 \end{cases}. \quad (23)$$

The corresponding contravariant base vectors are defined as

$$\mathbf{G}^i = G^{ij} \mathbf{G}_j \quad \text{and} \quad \mathbf{g}^i = g^{ij} \mathbf{g}_j, \quad (24)$$

where the contravariant metric coefficients G^{ij} and g^{ij} are given by

$$G^{ij} = [G_{ij}]^{-1} \quad \text{and} \quad g^{ij} = [g_{ij}]^{-1}, \quad (25)$$

with G_{ij} and g_{ij} , the covariant metric coefficients, defined as

$$G_{ij} = \mathbf{G}_i \cdot \mathbf{G}_j \quad \text{and} \quad g_{ij} = \mathbf{g}_i \cdot \mathbf{g}_j. \quad (26)$$

Similarly, the covariant and contravariant metric coefficients on the midsurfaces are defined as

$$\begin{cases} A_{ij} = \mathbf{A}_i \cdot \mathbf{A}_j \\ A^{ij} = [A_{ij}]^{-1} \end{cases} \quad \text{and} \quad \begin{cases} a_{ij} = \mathbf{a}_i \cdot \mathbf{a}_j \\ a^{ij} = [a_{ij}]^{-1} \end{cases}. \quad (27)$$

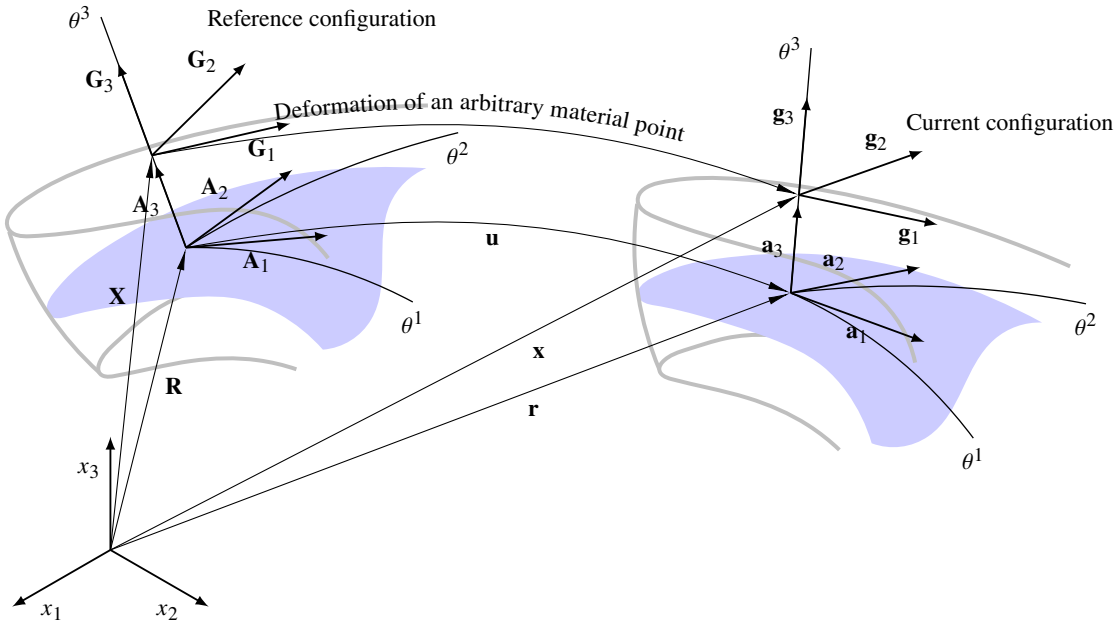


Figure 2: Schematics of the reference and current configurations of Kirchhoff-Love shells. The midsurfaces are highlighted by blue color.

The Green-Lagrange strain tensor, \mathbf{E} , can be written as

$$\mathbf{E} = E_{ij} \mathbf{G}^i \otimes \mathbf{G}^j, \quad (28)$$

where

$$E_{ij} = \frac{1}{2} (g_{ij} - G_{ij}). \quad (29)$$

Substituting (25) and (26) into (29) and neglecting $\mathcal{O}((\theta^3)^2)$ terms as the thickness is relatively small, we obtain the non-zero strain components as

$$E_{\alpha\beta} = \epsilon_{\alpha\beta} + \theta^3 \kappa_{\alpha\beta}, \quad (30)$$

where

$$\epsilon_{\alpha\beta} = \frac{1}{2} (\mathbf{a}_\alpha \cdot \mathbf{a}_\beta - \mathbf{A}_\alpha \cdot \mathbf{A}_\beta) \quad \text{and} \quad \kappa_{\alpha\beta} = -\mathbf{a}_{\alpha,\beta} \cdot \mathbf{a}_3 + \mathbf{A}_{\alpha,\beta} \cdot \mathbf{A}_3 \quad (31)$$

are the components of the membrane and bending strains, ϵ and κ , respectively.

3.2 Variational form of Kirchhoff-Love shell

For the sake of simplicity, we assume Saint-Venant Kirchhoff materials are used and the strain energy density per unit area for Kirchhoff-Love shells [52] is given by

$$W(\theta^1, \theta^2) = \frac{1}{2} \left(h \boldsymbol{\epsilon} : \mathbf{C} : \boldsymbol{\epsilon} + \frac{h^3}{12} \boldsymbol{\kappa} : \mathbf{C} : \boldsymbol{\kappa} \right) = \frac{1}{2} \left(h C^{\alpha\beta\gamma\delta} \epsilon_{\alpha\beta} \epsilon_{\gamma\delta} + \frac{h^3}{12} C^{\alpha\beta\gamma\delta} \kappa_{\alpha\beta} \kappa_{\gamma\delta} \right), \quad (32)$$

where E is Young's modulus, ν is Poisson's ratio and \mathbf{C} is the material tensor defined as

$$\mathbf{C} = C^{\alpha\beta\gamma\delta} \mathbf{A}_\alpha \otimes \mathbf{A}_\beta \otimes \mathbf{A}_\gamma \otimes \mathbf{A}_\delta, \quad C^{\alpha\beta\gamma\delta} = \frac{E\nu}{1-\nu^2} A^{\alpha\beta} A^{\gamma\delta} + \frac{E}{2(1+\nu)} \left(A^{\alpha\gamma} A^{\beta\delta} + A^{\alpha\delta} A^{\beta\gamma} \right). \quad (33)$$

The potential energy of Kirchhoff-Love shells can then be calculated by

$$\Pi(\mathbf{u}) = \Pi^{\text{int}}(\mathbf{u}) + \Pi^{\text{ext}}(\mathbf{f}, \mathbf{u}) = \int_{\bar{\Omega}} W d\Omega + \Pi^{\text{ext}}(\mathbf{f}, \mathbf{u}), \quad (34)$$

where $\bar{\Omega}$ is the midsurface of the shell in the reference configuration, $d\Omega = |\mathbf{A}_1 \times \mathbf{A}_2| d\theta^1 d\theta^2$ is the differential area, $\Pi^{\text{int}}(\mathbf{u}) = \int_{\bar{\Omega}} W d\Omega$ is the strain energy and $\Pi^{\text{ext}}(\mathbf{f}, \mathbf{u})$ is the external work due to external force \mathbf{f} . In general Π^{ext} is a linear functional with respect to \mathbf{u} . The variation formulation can be derived as the stationary point of the minimization of the potential energy as

$$\delta\Pi(\mathbf{u}, \delta\mathbf{u}) = \frac{\partial\Pi}{\partial\mathbf{u}} \delta\mathbf{u} = \int_{\bar{\Omega}} \delta\boldsymbol{\epsilon}(\mathbf{u}, \delta\mathbf{u}) : \mathbf{n}(\mathbf{u}) + \delta\boldsymbol{\kappa}(\mathbf{u}, \delta\mathbf{u}) : \mathbf{m}(\mathbf{u}) d\Omega + \Pi^{\text{ext}}(\mathbf{f}, \delta\mathbf{u}) = 0 \quad (35)$$

where $\delta\boldsymbol{\epsilon}$ and $\delta\boldsymbol{\kappa}$ are the first variation of the membrane and bending strains given as

$$\delta\boldsymbol{\epsilon}(\mathbf{u}, \delta\mathbf{u}) = \frac{\partial\boldsymbol{\epsilon}(\mathbf{u})}{\partial\mathbf{u}} \delta\mathbf{u} \quad \text{and} \quad \delta\boldsymbol{\kappa}(\mathbf{u}, \delta\mathbf{u}) = \frac{\partial\boldsymbol{\kappa}(\mathbf{u})}{\partial\mathbf{u}} \delta\mathbf{u}, \quad (36)$$

and \mathbf{n} and \mathbf{m} are the membrane force and bending moment resultant tensors written as

$$\begin{cases} \mathbf{n} = n^{\alpha\beta} \mathbf{A}_\alpha \otimes \mathbf{A}_\beta, & n^{\alpha\beta} = \frac{\partial W}{\partial \epsilon_{\alpha\beta}} = h C^{\alpha\beta\gamma\delta} \epsilon_{\gamma\delta} \\ \mathbf{m} = m^{\alpha\beta} \mathbf{A}_\alpha \otimes \mathbf{A}_\beta, & m^{\alpha\beta} = \frac{\partial W}{\partial \kappa_{\alpha\beta}} = \frac{h^3}{12} C^{\alpha\beta\gamma\delta} \kappa_{\gamma\delta} \end{cases}. \quad (37)$$

The variational formulation (35) is a nonlinear functional with respect to displacement \mathbf{u} which has to be linearized and solved iteratively. Assuming $\mathbf{u}^{i+1} = \mathbf{u}^i + \Delta\mathbf{u}$, the linearized formulation can be stated as: find $\Delta\mathbf{u} \in \mathcal{X}$, such that

$$(K_m(\mathbf{u}^i, \delta\mathbf{u}, \Delta\mathbf{u}) + K_b(\mathbf{u}^i, \delta\mathbf{u}, \Delta\mathbf{u})) = -\delta\Pi(\mathbf{u}^i, \delta\mathbf{u}), \quad \forall \delta\mathbf{u} \in \mathcal{X}, \quad (38)$$

where i denotes the i -th iterative step, the solution space $\mathcal{X} = [H^2(\Omega)]^3$, the membrane stiffness

$$K_m(\mathbf{u}^i, \delta\mathbf{u}, \Delta\mathbf{u}) = \int_{\bar{\Omega}} \delta\boldsymbol{\epsilon}(\mathbf{u}^i, \delta\mathbf{u}) : \delta\mathbf{n}(\mathbf{u}^i, \Delta\mathbf{u}) + \delta\boldsymbol{\epsilon}(\mathbf{u}^i, \delta\mathbf{u}) : \mathbf{n}(\mathbf{u}^i) d\Omega, \quad (39)$$

and the bending stiffness

$$K_b(\mathbf{u}^i, \delta\mathbf{u}, \Delta\mathbf{u}) = \int_{\bar{\Omega}} \delta\boldsymbol{\kappa}(\mathbf{u}^i, \delta\mathbf{u}) : \delta\mathbf{m}(\mathbf{u}^i, \Delta\mathbf{u}) + \delta\boldsymbol{\kappa}(\mathbf{u}^i, \delta\mathbf{u}) : \mathbf{m}(\mathbf{u}^i) d\Omega, \quad (40)$$

where

$$\begin{cases} \delta\mathbf{n}(\mathbf{u}, \Delta\mathbf{u}) = \frac{\partial\mathbf{n}(\mathbf{u})}{\partial\mathbf{u}} \Delta\mathbf{u} = h\mathbf{C} : \delta\boldsymbol{\epsilon}(\mathbf{u}, \Delta\mathbf{u}), \\ \delta\mathbf{m}(\Delta\mathbf{u}) = \frac{\partial\mathbf{m}}{\partial\mathbf{u}} \Delta\mathbf{u} = \frac{h^3}{12} \mathbf{C} : \delta\boldsymbol{\kappa}(\Delta\mathbf{u}), \\ \delta\boldsymbol{\epsilon}(\mathbf{u}, \delta\mathbf{u}, \Delta\mathbf{u}) = \frac{\partial\delta\boldsymbol{\epsilon}(\mathbf{u}, \delta\mathbf{u})}{\partial\mathbf{u}} \Delta\mathbf{u}, \\ \delta\boldsymbol{\kappa}(\mathbf{u}, \delta\mathbf{u}, \Delta\mathbf{u}) = \frac{\partial\delta\boldsymbol{\kappa}(\mathbf{u}, \delta\mathbf{u})}{\partial\mathbf{u}} \Delta\mathbf{u}. \end{cases} \quad (41)$$

4 A dual mortar formulation for the multi-patch Kirchhoff-Love shell

In this section we present a dual mortar formulation for coupling multi-patch Kirchhoff-Love shells. Thanks to the locally supported dual basis, the linear system can be statically condensed with minimum computational cost and the resulting linear system preserves its sparsity. Along each interface, we introduce a local coordinate system, in which an inter-patch constraint is developed in a natural manner. This inter-patch constraint is dual compatible in the sense that when the Lagrange multiplier is discretized by the dual basis functions the resulted constraint matrix has the form of (13). It also gives a unified framework for coupling patches that are joined together either with G^1 -continuity or with a kink.

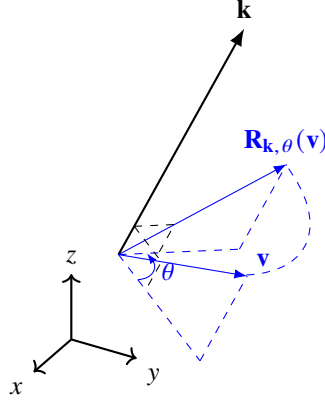


Figure 3: Rodrigues' rotation operator $\mathbf{R}_{\mathbf{k},\theta}$ rotates \mathbf{v} by an angle θ around \mathbf{k} following the right-hand rule.

We first introduce a rotation operator (see Figure 3): for a vector $\mathbf{v} \in \mathbb{R}^3$, its rotation around the axis $\mathbf{k} \in \mathbb{R}^3$ by an angle θ according to the right hand rule is given as

$$\mathbf{R}_{\mathbf{k},\theta}(\mathbf{v}) = \mathbf{v} \cos(\theta) + \left(\frac{\mathbf{k}}{|\mathbf{k}|} \times \mathbf{v} \right) \sin(\theta) + \frac{\mathbf{k}}{|\mathbf{k}|} \left(\frac{\mathbf{k}}{|\mathbf{k}|} \cdot \mathbf{v} \right) (1 - \cos(\theta)). \quad (42)$$

This operator is called the Rodrigues' rotation formula [53] and will play an important rule in formulating the inter-patch constraint.

To demonstrate our approach, we consider a kinked shell structure consisting of two NURBS patches shown in Figure 5, where Ω_s denotes the slave domain, Ω_m the master domain and Γ the intersection between two patches. These two domains are parameterized by coordinate systems (θ_s^1, θ_s^2) and (θ_m^1, θ_m^2) , respectively.

4.1 A local coordinate system for patch intersections

Table 1: A summary of the restriction of $\bar{\theta}^1$ and $\bar{\theta}^2$ on Ω_s for different coupling orientation and corresponding Jacobians.

Interface orientation	$\bar{\theta}_s^1$	$\bar{\theta}_s^2$	$\mathbf{J}_{\bar{\theta}_s^1}$	$\mathbf{J}_{\bar{\theta}_s^2}$
South	$\bar{\mathbf{A}}_1^s = -\mathbf{A}_2^s$	$\bar{\mathbf{A}}_2^s = \mathbf{A}_1^s$	$\begin{bmatrix} 0 & -1 \end{bmatrix}^T$	$\begin{bmatrix} 1 & 0 \end{bmatrix}^T$
East	$\bar{\mathbf{A}}_1^s = \mathbf{A}_1^s$	$\bar{\mathbf{A}}_2^s = \mathbf{A}_2^s$	$\begin{bmatrix} 1 & 0 \end{bmatrix}^T$	$\begin{bmatrix} 0 & 1 \end{bmatrix}^T$
North	$\bar{\mathbf{A}}_1^s = \mathbf{A}_2^s$	$\bar{\mathbf{A}}_2^s = -\mathbf{A}_1^s$	$\begin{bmatrix} 0 & 1 \end{bmatrix}^T$	$\begin{bmatrix} -1 & 0 \end{bmatrix}^T$
West	$\bar{\mathbf{A}}_1^s = -\mathbf{A}_1^s$	$\bar{\mathbf{A}}_2^s = -\mathbf{A}_2^s$	$\begin{bmatrix} -1 & 0 \end{bmatrix}^T$	$\begin{bmatrix} 0 & -1 \end{bmatrix}^T$

In this subsection, we reparameterize the intersection between the slave patch and the master patch by a new coordinate system $(\bar{\theta}^1, \bar{\theta}^2)$, whose restriction to the slave and master patches are denoted by $(\bar{\theta}_s^1, \bar{\theta}_s^2)$ and $(\bar{\theta}_m^1, \bar{\theta}_m^2)$, respectively. The associated covariant base vectors of these three different representations of this new coordinate system are denoted as $(\bar{\mathbf{A}}_1, \bar{\mathbf{A}}_2)$, $(\bar{\mathbf{A}}_1^s, \bar{\mathbf{A}}_2^s)$, and $(\bar{\mathbf{A}}_1^m, \bar{\mathbf{A}}_2^m)$, respectively. The main reason for the reparameterization of the intersection is to simplify the formulation of the dual compatible continuity constraint that will be shown in the

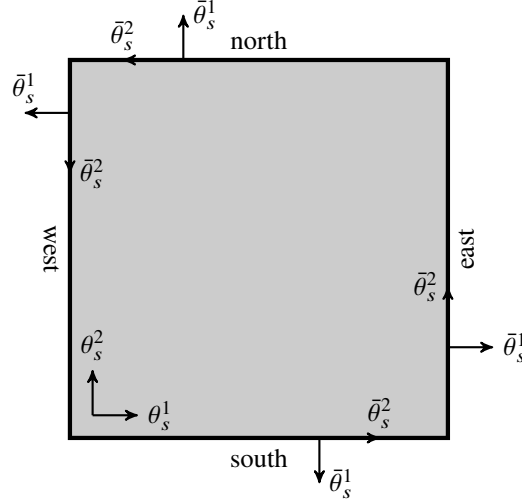


Figure 4: The new coordinate system $(\bar{\theta}^1, \bar{\theta}^2)$ on the parametric domain of the slave patch. Coordinate systems on different edges denote the orientations in different coupling scenarios. Note that no matter which edge is coupled, $\bar{\mathbf{A}}_3^s$ always coincides with \mathbf{A}_3^s .

following subsection. Under the new coordinate system, the dual compatible continuity constraint will be independent of the local coordinate systems on both slave and master patches.

The covariant base vectors $(\bar{\mathbf{A}}_1, \bar{\mathbf{A}}_2)$ are first developed on the slave patch side and then extended to the master patch side. On the slave patch side, $(\bar{\mathbf{A}}_1^s, \bar{\mathbf{A}}_2^s)$ is defined based on the following principles:

- $\bar{\mathbf{A}}_1^s$ is colinear to either the director \mathbf{A}_1^s or \mathbf{A}_2^s , and it points outward of Ω_s .
- $\bar{\mathbf{A}}_2^s$ is coplanar to the director \mathbf{A}_1^s and \mathbf{A}_2^s and is generated through rotating $\bar{\mathbf{A}}_1^s$ by 90° in the counterclockwise direction.
- $\bar{\mathbf{A}}_3^s = \frac{\bar{\mathbf{A}}_1^s \times \bar{\mathbf{A}}_2^s}{|\bar{\mathbf{A}}_1^s \times \bar{\mathbf{A}}_2^s|}$ coincides with \mathbf{A}_3^s .

These principles allow us to take the advantage of the tensor product structure of spline basis and endow dual compatibility to constraints that involve partial derivative terms. The relations between $\bar{\mathbf{A}}_\alpha^s$ and \mathbf{A}_α^s are tabulated in Table 1 for parametric boundaries, and the new local coordinate systems are illustrated in Figure 4. The mapping from \mathbf{A}_α^s to $\bar{\mathbf{A}}_\alpha^s$ can be represented by

$$\begin{cases} \bar{\mathbf{A}}_1^s = \frac{\partial \mathbf{X}^s}{\partial \bar{\theta}^1 |_{\Omega_s}} = [\mathbf{A}_1^s & \mathbf{A}_2^s] \cdot \mathbf{J}_{\bar{\theta}^1} \\ \bar{\mathbf{A}}_2^s = \frac{\partial \mathbf{X}^s}{\partial \bar{\theta}^2 |_{\Omega_s}} = [\mathbf{A}_1^s & \mathbf{A}_2^s] \cdot \mathbf{J}_{\bar{\theta}^2} \end{cases}, \quad (43)$$

where the Jacobians

$$\begin{cases} \mathbf{J}_{\bar{\theta}^1} |_{\Omega_s} = \begin{bmatrix} \frac{\partial \theta_s^1}{\partial \bar{\theta}^1} \\ \frac{\partial \theta_s^2}{\partial \bar{\theta}^1} \end{bmatrix} \\ \mathbf{J}_{\bar{\theta}^2} |_{\Omega_s} = \begin{bmatrix} \frac{\partial \theta_s^1}{\partial \bar{\theta}^2} \\ \frac{\partial \theta_s^2}{\partial \bar{\theta}^2} \end{bmatrix} \end{cases} \quad (44)$$

are given in Table 1 for different parametric boundaries.

We now extend the curvilinear coordinate system $(\bar{\theta}^1, \bar{\theta}^2)$ from the slave patch to the master patch by rotating $\bar{\mathbf{A}}_1^s$ and $\bar{\mathbf{A}}_2^s$ onto the tangential plane of Ω_m about the intersection. Since $\bar{\mathbf{A}}_2^s$ is colinear with the intersection, it is invariant with any rotations about itself:

$$\bar{\mathbf{A}}_2^m = \bar{\mathbf{A}}_2^s. \quad (45)$$

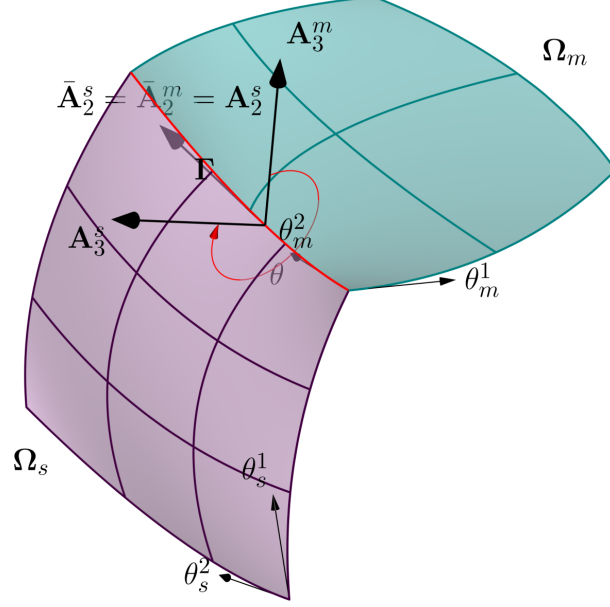


Figure 5: A two-patch non-conforming Kirchhoff-Love shell consisting of two patches Ω_s and Ω_m with the intersection denoted by the red curve. The directors \mathbf{A}_3^m , \mathbf{A}_3^s and \mathbf{A}_2^s determine a rotation angle θ along the intersection.

Given the directors \mathbf{A}_3^s and \mathbf{A}_3^m and the axis $\bar{\mathbf{A}}_2^m$, we can now uniquely determine the rotation angle θ (see Figure 5) from \mathbf{A}_3^m to \mathbf{A}_3^s by

$$\begin{cases} \cos \theta = \mathbf{A}_3^m \cdot \mathbf{A}_3^s \\ \sin \theta = \frac{(\mathbf{A}_3^m \times \mathbf{A}_3^s) \cdot \bar{\mathbf{A}}_2^m}{|\bar{\mathbf{A}}_2^m|}. \end{cases} \quad (46)$$

By Equation (42), we can define two rotation operators about the axis $\bar{\mathbf{A}}_2^m$ such that

$$\mathbf{A}_3^s = \mathbf{R}_{\bar{\mathbf{A}}_2^m, \theta}(\mathbf{A}_3^m) \quad \text{and} \quad \mathbf{A}_3^m = \mathbf{R}_{\bar{\mathbf{A}}_2^m, -\theta}(\mathbf{A}_3^s). \quad (47)$$

Meanwhile, the rotation operator $\mathbf{R}_{\bar{\mathbf{A}}_2^m, -\theta}$ rotates $\bar{\mathbf{A}}_1^s$ to the tangential plane of Ω_m along the intersection (see Figure 6). We let

$$\bar{\mathbf{A}}_1^m = \mathbf{R}_{\bar{\mathbf{A}}_2^m, -\theta}(\bar{\mathbf{A}}_1^s). \quad (48)$$

The corresponding Jacobians $\mathbf{J}_{\bar{\theta}_m^1} = \begin{bmatrix} \frac{\partial \theta_m^1}{\partial \theta_m^1} & \frac{\partial \theta_m^2}{\partial \theta_m^1} \end{bmatrix}^T$ and $\mathbf{J}_{\bar{\theta}_m^2} = \begin{bmatrix} \frac{\partial \theta_m^1}{\partial \theta_m^2} & \frac{\partial \theta_m^2}{\partial \theta_m^2} \end{bmatrix}^T$ are given by

$$\begin{aligned} \begin{bmatrix} \mathbf{A}_1^m & \mathbf{A}_2^m \end{bmatrix} \cdot \mathbf{J}_{\bar{\theta}_m^1} &= \bar{\mathbf{A}}_1^m = \mathbf{R}_{\bar{\mathbf{A}}_2^m, -\theta}(\bar{\mathbf{A}}_1^s), \\ \begin{bmatrix} \mathbf{A}_1^m & \mathbf{A}_2^m \end{bmatrix} \cdot \mathbf{J}_{\bar{\theta}_m^2} &= \bar{\mathbf{A}}_2^m = \bar{\mathbf{A}}_2^s. \end{aligned} \quad (49)$$

As $\begin{bmatrix} \mathbf{A}_1^m & \mathbf{A}_2^m \end{bmatrix}$ is a 3×2 matrix, Equation (49) could not be factorized directly. However, as $\mathbf{R}_{\bar{\mathbf{A}}_2^m, -\theta}(\bar{\mathbf{A}}_1^s)$ and $\bar{\mathbf{A}}_2^s$ are on the tangential plane of Ω_m , we can solve $\mathbf{J}_{\bar{\theta}_m^1}$ and $\mathbf{J}_{\bar{\theta}_m^2}$ exactly by

$$\begin{aligned} \mathbf{J}_{\bar{\theta}_m^1} &= \left(\begin{bmatrix} \mathbf{A}_1^m & \mathbf{A}_2^m \end{bmatrix}^T \cdot \begin{bmatrix} \mathbf{A}_1^m & \mathbf{A}_2^m \end{bmatrix} \right)^{-1} \left(\begin{bmatrix} \mathbf{A}_1^m & \mathbf{A}_2^m \end{bmatrix}^T \cdot \mathbf{R}_{\bar{\mathbf{A}}_2^m, -\theta}(\bar{\mathbf{A}}_1^s) \right), \\ \mathbf{J}_{\bar{\theta}_m^2} &= \left(\begin{bmatrix} \mathbf{A}_1^m & \mathbf{A}_2^m \end{bmatrix}^T \cdot \begin{bmatrix} \mathbf{A}_1^m & \mathbf{A}_2^m \end{bmatrix} \right)^{-1} \left(\begin{bmatrix} \mathbf{A}_1^m & \mathbf{A}_2^m \end{bmatrix}^T \cdot \bar{\mathbf{A}}_2^s \right). \end{aligned} \quad (50)$$

The partial derivatives of the displacement \mathbf{u} w.r.t. the new coordinate system $(\bar{\theta}^1, \bar{\theta}^2)$ along the intersection are

now given by

$$\begin{cases} \bar{\mathbf{u}}_{,1}^s = \frac{\partial \mathbf{u}^s}{\partial \bar{\theta}_s^1} = [\mathbf{u}_{,1}^s & \mathbf{u}_{,2}^s] \mathbf{J}_{\bar{\theta}_s^1} \\ \bar{\mathbf{u}}_{,2}^s = \frac{\partial \mathbf{u}^s}{\partial \bar{\theta}_s^2} = [\mathbf{u}_{,1}^s & \mathbf{u}_{,2}^s] \mathbf{J}_{\bar{\theta}_s^2} \\ \bar{\mathbf{u}}_{,1}^m = \frac{\partial \mathbf{u}^m}{\partial \bar{\theta}_m^1} = [\mathbf{u}_{,1}^m & \mathbf{u}_{,2}^m] \mathbf{J}_{\bar{\theta}_m^1} \\ \bar{\mathbf{u}}_{,2}^m = \frac{\partial \mathbf{u}^m}{\partial \bar{\theta}_m^2} = [\mathbf{u}_{,1}^m & \mathbf{u}_{,2}^m] \mathbf{J}_{\bar{\theta}_m^2} \end{cases} \quad (51)$$

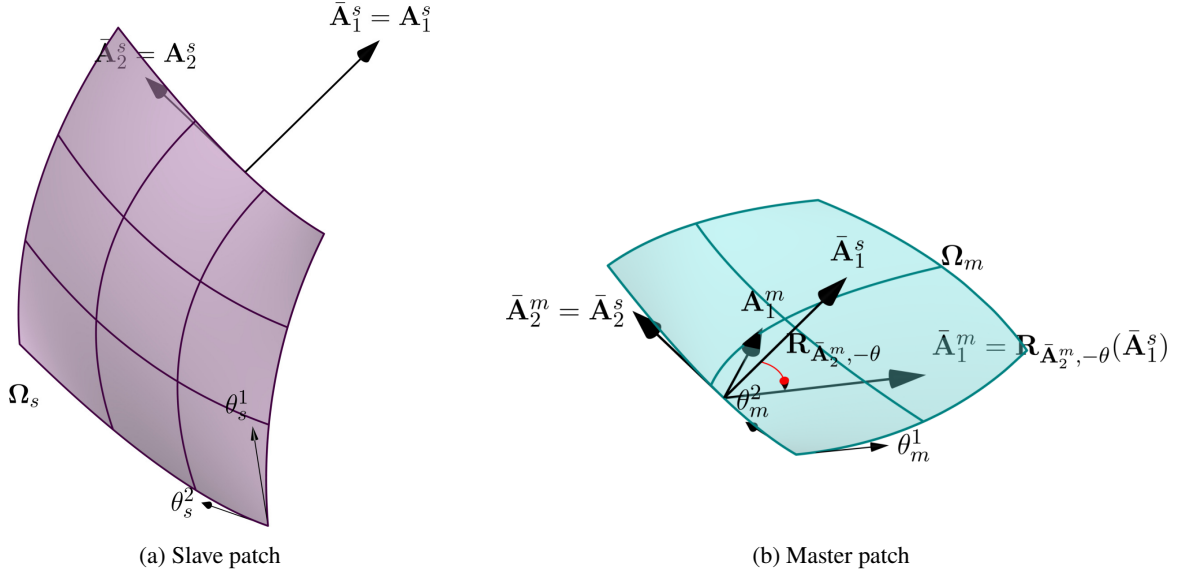


Figure 6: The covariant base vectors $(\bar{\mathbf{A}}_1^s, \bar{\mathbf{A}}_2^s)$ and $(\bar{\mathbf{A}}_1^m, \bar{\mathbf{A}}_2^m)$. Note that $(\bar{\mathbf{A}}_1^m, \bar{\mathbf{A}}_2^m)$ can be obtained by rotating $(\bar{\mathbf{A}}_1^s, \bar{\mathbf{A}}_2^s)$ via the rotation operator $\mathbf{R}_{\bar{\mathbf{A}}_2^m, -\theta}$.

4.2 A dual-compatible constraint for Kirchhoff-Love shell coupling

In this subsection, we propose a set of constraints that can handle Kirchhoff-Love shell coupling not only in a systematic, but also a novel manner as well. Many existing definitions of coupling constraints are not sufficient to handle all coupling scenarios. For instance, the constraint proposed in [43] can only enforce coupling constraints on G^1 -continuous patches, which precludes its application to coupling multiple patches with kinks. Another example is the constraint used in [54, 42], which is only designed for small deformation problems. In contrast, our proposed constraints can handle all of these cases in a consistent way. If multi-patch geometry is G^1 -continuous along patch interfaces, the proposed constraints will enforce C^1 continuity across adjacent patches. If patches are joined at kinks, the angles between directors of adjacent patches will be preserved. In addition, the proposed constraints are dual compatible, i.e. when the Lagrange multipliers are discretized by dual basis functions, the discretized constraint matrix takes the form of Equation (13). Hence, the *inf-sup* stability is automatically satisfied.

The basic C^0 -continuous constraint of the displacement field between the slave and master patches must be satisfied in the current configuration, i.e.,

$$\mathbf{r}^s - \mathbf{r}^m = 0. \quad (52)$$

The continuity constraint (52) only prevents adjacent patches from tearing apart. To transfer bending moment from one patch to another, the coupling constraints must also preserve the angle formed by adjacent patches. Hence, the following rotational constraint is also applied in the current configuration:

$$\bar{\mathbf{a}}_1^s - \mathbf{R}_{\bar{\mathbf{a}}_2^m, \theta}(\bar{\mathbf{a}}_1^m) = 0. \quad (53)$$

Note that, although a rotational constraint between the director \mathbf{a}_2^s and \mathbf{a}_3^m is more straightforward for imposing rotational continuity, Equation (53) leads to a dual compatible constraint, as explained in Remark 1. The reason why $\bar{\mathbf{a}}_2^m$ is chosen as the rotation axis is given in Remark 2.

Subtracting Equation (52) and Equation (53) by their reference configuration counterparts, we obtain the continuity constraints in terms of the displacement field:

$$\mathbf{u}^s - \mathbf{u}^m = 0, \quad (54a)$$

$$\bar{\mathbf{u}}_{,1}^s - \mathbf{R}_{\bar{\mathbf{a}}_2^m, \theta}(\bar{\mathbf{a}}_1^m) + \mathbf{R}_{\bar{\mathbf{A}}_2^m, \theta}(\bar{\mathbf{A}}_1^m) = 0. \quad (54b)$$

Note that, for two patches that meet at the interface with G^1 -continuity, i.e. $\theta = 0$, Equation (54b) reduces to

$$\bar{\mathbf{u}}_{,1}^s - \mathbf{R}_{\bar{\mathbf{a}}_2^m, 0}(\bar{\mathbf{a}}_1^m) + \mathbf{R}_{\bar{\mathbf{A}}_2^m, 0}(\bar{\mathbf{A}}_1^m) = \bar{\mathbf{u}}_{,1}^s - \bar{\mathbf{a}}_1^m + \bar{\mathbf{A}}_1^m = \bar{\mathbf{u}}_{,1}^s - \bar{\mathbf{u}}_{,1}^m = 0, \quad (55)$$

which is indeed the C^1 continuity condition in the coordinate system $(\bar{\theta}^1, \bar{\theta}^2)$. Both Equation (54a) and Equation (55) are linear. To solve the nonlinear problem at $\mathbf{u}^{i+1} = \mathbf{u}^i + \Delta\mathbf{u}$, we have

$$\Delta\mathbf{u}^s - \Delta\mathbf{u}^m = 0, \quad (56a)$$

$$\Delta\bar{\mathbf{u}}_{,1}^s - \Delta\bar{\mathbf{u}}_{,1}^m = 0. \quad (56b)$$

However, when patches meet at a kink, the rotational constraint (54b) is no longer linear. Hence, the Newton-Raphson method is needed to apply to the constraint iteratively as

$$\Delta\bar{\mathbf{u}}_{,1}^s - \frac{\partial \mathbf{R}_{\bar{\mathbf{a}}_2^m, \theta}(\bar{\mathbf{a}}_1^m)}{\partial \mathbf{u}^m} \Delta\bar{\mathbf{u}}^m = \mathbf{r}_c^i, \quad \text{with } \mathbf{r}_c^i = - \left[\bar{\mathbf{a}}_1^s - \mathbf{R}_{\bar{\mathbf{a}}_2^m, \theta}(\bar{\mathbf{a}}_1^m) \right]_{\mathbf{u}=\mathbf{u}^i}. \quad (57)$$

Remark 1. When the constraint (57) is applied weakly through Lagrange multiplier method and the Lagrange multipliers are chosen to be the enriched dual basis functions of the slave interface basis functions, the biorthogonality relation between $\Delta\bar{\mathbf{u}}_{,1}^s$ and the Lagrange multipliers is preserved up to a constant. For instance, assume without loss of generality that the intersection is the east edge of the slave patch ($\theta_s^1 = 1$). Then the new coordinate $\bar{\theta}_s^1$ is θ_s^1 , and an arbitrary term appearing in the evaluation of the integral $\int_{\Gamma} \Delta\bar{\mathbf{u}}_{,1}^s \cdot \delta\lambda d\Gamma$ can be calculated as

$$\begin{aligned} \int_{\Gamma} \frac{\partial N_a(\theta_s^1, \theta_s^2)}{\partial \theta_s^1} \hat{N}_k(\theta_s^2) d\Gamma &= \int_{\Gamma} \frac{\partial N_i(1) N_j(\theta_s^2)}{\partial \theta_s^1} \hat{N}_k(\theta_s^2) d\Gamma \\ &= \frac{\partial N_i(1)}{\partial \theta_s^1} \int_{\Gamma} N_j(\theta_s^2) \hat{N}_k(\theta_s^2) d\Gamma \quad i \in \{1, 2, \dots, n_{\theta_s^1}\} \quad j, k \in \{1, 2, \dots, n_{\theta_s^2}\}, \\ &= \frac{\partial N_i(1)}{\partial \theta_s^1} \delta_{jk} \end{aligned} \quad (58)$$

where $n_{\theta_s^1}$ and $n_{\theta_s^2}$ are the number of nodes in the θ_s^1 and θ_s^2 directions of the slave patch, respectively, Γ is the parametric domain of the intersection, $N_a(\theta_s^1, \theta_s^2) = N_i(\theta_s^1) N_j(\theta_s^2)$ is a nodal basis function of the slave patch and $\hat{N}_k(\theta_s^2)$ is a dual basis function of the trace space of the intersection, i.e. $\int_{\Gamma} N_j(\theta_s^2) \hat{N}_k(\theta_s^2) d\Gamma = \delta_{jk}$. Here the biorthogonality relation is preserved up to a constant $\frac{\partial N_i(1)}{\partial \theta_s^1}$.

Remark 2. It is important to use $\bar{\mathbf{a}}_2^m$ as the rotation axis in the rotation operator formulation of Equation (53). Although $\bar{\mathbf{a}}_2^s$ equals to $\bar{\mathbf{a}}_2^m$ in the weak sense, the presence of $\Delta\bar{\mathbf{u}}_{,2}^s$ in the linearization of $\bar{\mathbf{a}}_2^m$ will impede the formulation of the identity submatrix in Equation (13).

4.3 The dual mortar formulation

The Lagrange multiplier formulation for the multi-patch nonlinear Kirchhoff-Love shell can be stated as: find $\Delta\mathbf{u} \in \mathcal{X}$, $\lambda_0 \in \mathcal{M}_0$ and $\lambda_1 \in \mathcal{M}_1$ such that

$$\left\{ \begin{aligned} K_m(\mathbf{u}^i, \delta\mathbf{u}, \Delta\mathbf{u}) + K_b(\mathbf{u}^i, \delta\mathbf{u}, \Delta\mathbf{u}) + b_0(\lambda_0, \delta\mathbf{u}) + b_1(\mathbf{u}^i, \lambda_1, \delta\mathbf{u}) &= -\delta\Pi(\mathbf{u}^i, \delta\mathbf{u}) \quad \forall \delta\mathbf{u} \in \mathcal{X}, \end{aligned} \right. \quad (59a)$$

$$b_0(\delta\lambda_0, \Delta\mathbf{u}) = 0 \quad \forall \delta\lambda_0 \in \mathcal{M}_0, \quad (59b)$$

$$b_1(\mathbf{u}^i, \delta\lambda_1, \Delta\mathbf{u}) = R_{b_1}(\mathbf{u}^i, \delta\lambda_1) \quad \forall \delta\lambda_1 \in \mathcal{M}_1, \quad (59c)$$

where

$$b_0(\delta\lambda_0, \Delta\mathbf{u}) = \sum_{\Gamma \in \mathbf{S}} \int_{\Gamma} \delta\lambda_0 \cdot (\Delta\mathbf{u}^s - \Delta\mathbf{u}^m) d\Gamma, \quad (60a)$$

$$b_1(\mathbf{u}^i, \delta\lambda_1, \Delta\mathbf{u}) = \sum_{\Gamma \in \mathbf{S}} \int_{\Gamma} \delta\lambda_1 \cdot \left(\Delta\bar{\mathbf{u}}_{,1}^s - \frac{\partial \mathbf{R}_{\bar{\mathbf{a}}_2^m, \theta(\bar{\mathbf{a}}_1^m)}}{\partial \mathbf{u}^m} \Delta\bar{\mathbf{u}}^m \right) d\Gamma, \quad (60b)$$

$$R_{b_1}(\mathbf{u}^i, \delta\lambda_1) = \sum_{\Gamma \in \mathbf{S}} \int_{\Gamma} \delta\lambda_1 \cdot \mathbf{r}_c^i d\Gamma, \quad (60c)$$

where \mathbf{S} is the union of all interfaces. The constrained function space for the dual mortar formulation of the multi-patch Kirchhoff-Love shell problem can then be defined as

$$\mathcal{V} := \{ \Delta\mathbf{v} \in \mathcal{X} \mid b_0(\boldsymbol{\mu}_0, \Delta\mathbf{v}) = 0 \text{ and } b_1(\mathbf{u}^i, \boldsymbol{\mu}_1, \Delta\mathbf{v}) = R_{b_1}(\mathbf{u}^i, \boldsymbol{\mu}_1), \quad \forall (\boldsymbol{\mu}_0, \boldsymbol{\mu}_1) \in \mathcal{M}_0 \times \mathcal{M}_1 \}. \quad (61)$$

The dual mortar formulation for the multi-patch Kirchhoff-Love shell can then be stated as: find $\Delta\mathbf{u} = \Delta\mathbf{u}_{\text{non}} + \Delta\mathbf{u}_{\text{hom}}$, with the homogeneous contribution $\Delta\mathbf{u}_{\text{hom}} \in \mathcal{V}$ such that

$$K_m(\mathbf{u}^i, \delta\mathbf{u}, \Delta\mathbf{u}) + K_b(\mathbf{u}^i, \delta\mathbf{u}, \Delta\mathbf{u}) = -\delta\Pi(\mathbf{u}^i, \delta\mathbf{u}), \quad \forall \delta\mathbf{u} \in \mathcal{V}, \quad (62)$$

where the non-homogeneous contribution $\Delta\mathbf{u}_{\text{non}}$ is a function in \mathcal{X} that satisfies both constraint (59b) and (59c).

In what follows, we will show that in the dual mortar formulation the constrained function space \mathcal{V} and the non-homogeneous contribution $\Delta\mathbf{u}_{\text{non}}$ can be constructed with minimum computational costs.

4.4 Discretization

Let Ω be subdivided into K non-overlapping subdomains Ω_k , $1 \leq k \leq K$. To approximate the solution of the variational problem (62), we discretize each subdomain by B-spline basis functions $\{N_i\}_{i \in I_k}$, where I_k is the index set for subdomain Ω_k . The incremental displacement and its variation are discretized as

$$\Delta\mathbf{u}^h = \sum_{i \in \cup_{k=1}^K I_k} \mathbf{N}_i \cdot \Delta\mathbf{U}_i, \quad \delta\mathbf{u}^h = \sum_{i \in \cup_{k=1}^K I_k} \mathbf{N}_i \cdot \delta\mathbf{U}_i, \quad (63)$$

where

$$\delta\mathbf{U}_i = \begin{bmatrix} \delta U_i^x \\ \delta U_i^y \\ \delta U_i^z \end{bmatrix}, \quad \Delta\mathbf{U}_i = \begin{bmatrix} \Delta U_i^x \\ \Delta U_i^y \\ \Delta U_i^z \end{bmatrix}, \quad \mathbf{N}_i = \begin{bmatrix} N_i & 0 & 0 \\ 0 & N_i & 0 \\ 0 & 0 & N_i \end{bmatrix}. \quad (64)$$

The Lagrange multipliers and their variations are discretized by the dual basis of the discretized space of intersections. However, for a case of more than three patches sharing a common interior vertex, if we discretize the Lagrange multiplier space with the same dimension as the univariate basis of the slave side, we will obtain too many constraints. Nodes in the neighborhood of this kind of vertex may serve as both slave and master nodes and the matrix \mathbf{B}^\perp cannot be formed elegantly using (14). Hence, modifications to the Lagrange multiplier space in the neighborhood of this types of vertex are needed to relax the overly constrained linear system. Note that these modifications are also commonly called cross point modifications, for details see [55, 56].

In general, these vertex modifications can be achieved by reducing the dimension of the Lagrange multiplier space. Here, we consider a set of dual bases $\{\hat{N}_i\}_{i=1}^{\hat{n}}$ of codimension four of the corresponding $n_{\bar{\theta}_s^2}$ -dimensional trace space ($\hat{n} = n_{\bar{\theta}_s^2} - 4$) that satisfies the following biorthogonality relation

$$\int_{\Gamma} \hat{N}_i(\bar{\theta}^2) N_{j+2}(\bar{\theta}_s^2) d\Gamma = \delta_{ij}, \quad 1 \leq i, j - 2 \leq n_{\bar{\theta}_s^2} - 4. \quad (65)$$

where the choice of the basis functions $N_{j+2}^s(\bar{\theta}^2)$ of the trace space depends on the orientation and are summarized in Table 2. The codimension can be accomplished by coarsening the mesh in the neighborhood of each vertex. For the global dual basis, we remove the two knots adjacent to each vertex. For the enriched Bézier dual basis, there is a

Table 2: A summary of all parameters used in the description of the discretized Lagrange multiplier λ_0 and λ_1

Interface orientation	$N_j^s(\bar{\theta}^2)$	$n_{\bar{\theta}^2}^s$	c
South	$N_j^s(\theta^1)$	$n_{\theta^1}^s$	$-\frac{\partial N_2^s(\theta^2)}{\partial \theta^2} \Big _{\theta^2=0}$
East	$N_j^s(\theta^2)$	$n_{\theta^2}^s$	$\frac{\partial N_{n_{\theta^1}^s-1}^s(\theta^1)}{\partial \theta^1} \Big _{\theta^1=1}$
North	$N_j^s(\theta^1)$	$n_{\theta^1}^s$	$\frac{\partial N_{n_{\theta^2}^s-1}^s(\theta^2)}{\partial \theta^2} \Big _{\theta^2=1}$
West	$N_j^s(\theta^2)$	$n_{\theta^2}^s$	$-\frac{\partial N_2^s(\theta^1)}{\partial \theta^1} \Big _{\theta^1=0}$

built-in coarsening algorithm, see [35] for more details. The Lagrange multiplier vector λ_0 , λ_1 and their variation are written as:

$$\begin{aligned} \lambda_0^h &= \sum_{i=1}^{\hat{n}} \hat{\mathbf{N}}_i \cdot \Lambda_i^0, & \delta \lambda_0^h &= \sum_{i=1}^{\hat{n}} \hat{\mathbf{N}}_i \cdot \delta \Lambda_i^0, \\ \lambda_1^h &= \frac{1}{c} \sum_{i=1}^{\hat{n}} \hat{\mathbf{N}}_i \cdot \Lambda_i^1, & \delta \lambda_1^h &= \frac{1}{c} \sum_{i=1}^{\hat{n}} \hat{\mathbf{N}}_i \cdot \delta \Lambda_i^1, \end{aligned} \quad (66)$$

where

$$\Lambda_i^0 = \begin{bmatrix} \Lambda_i^{0x} \\ \Lambda_i^{0y} \\ \Lambda_i^{0z} \end{bmatrix}, \quad \delta \Lambda_i^0 = \begin{bmatrix} \delta \Lambda_i^{0x} \\ \delta \Lambda_i^{0y} \\ \delta \Lambda_i^{0z} \end{bmatrix}, \quad \Lambda_i^1 = \begin{bmatrix} \Lambda_i^{1x} \\ \Lambda_i^{1y} \\ \Lambda_i^{1z} \end{bmatrix}, \quad \delta \Lambda_i^1 = \begin{bmatrix} \delta \Lambda_i^{1x} \\ \delta \Lambda_i^{1y} \\ \delta \Lambda_i^{1z} \end{bmatrix}, \quad \hat{\mathbf{N}}_i = \begin{bmatrix} \hat{N}_i & 0 & 0 \\ 0 & \hat{N}_i & 0 \\ 0 & 0 & \hat{N}_i \end{bmatrix}, \quad (67)$$

and the weight c is given in Table 2. In the bilinear form b_0 , the biorthogonality relation is established between the Lagrange multiplier $\delta \lambda_0$ and all except the first and last two slave nodes on the intersection. In the bilinear form b_1 , the biorthogonality relation is established between the Lagrange multiplier $\delta \lambda_1$ and all except the first and last two slave nodes that are one column away from the intersection.

By substituting the discretized displacement field and Lagrange multipliers into the mixed problem (59), we obtain the following stiffness, constraint matrices and the right-hand side of the non-homogeneous constraint (59c):

$$\begin{aligned} \delta \mathbf{U}^T \mathbf{K} \Delta \mathbf{U} &= K_m(\mathbf{u}^{hi}, \delta \mathbf{u}^h, \Delta \mathbf{u}^h) + K_b(\mathbf{u}^{hi}, \delta \mathbf{u}^h, \Delta \mathbf{u}^h), \\ \begin{bmatrix} \delta \Lambda^0 \\ \delta \Lambda^1 \end{bmatrix}^T \mathbf{B} \Delta \mathbf{U} &= \begin{bmatrix} b_0(\delta \lambda_0^h, \Delta \mathbf{u}^h) \\ b_1(\mathbf{u}^{hi}, \delta \lambda_1^h, \Delta \mathbf{u}^h) \end{bmatrix}, \\ [\delta \Lambda^1]^T \mathbf{R}_{b_1} &= R_{b_1}(\mathbf{u}^{hi}, \delta \lambda_1^h). \end{aligned} \quad (68)$$

The structure of the discretized constraint matrix \mathbf{B} depends on the index sets $\{I_k\}_{k=1}^K$ and the ordering of the Lagrange multiplier basis functions. In order to recover the form of (13), we classify nodes, associated with basis functions, into slave, master and inactive nodes (see Figure 7). For slave nodes, we further subdivide them into two categories:

- I The second closest column of nodes to each intersection $\Gamma \in \mathbf{S}$, illustrated by blue dots as shown in Figure 7. They are biorthogonal to the associated Lagrange multiplier $\delta \lambda_1$ in the discretization of the bilinear form b_1 . Their indices are denoted by the index set I_s^I .
- II The column of nodes on the intersection $\Gamma \in \mathbf{S}$, illustrated by red dots as shown in Figure 7. They are biorthogonal to the associated Lagrange multiplier $\delta \lambda_0$ in the discretization of the bilinear form b_0 . Their indices are denoted by the index set I_s^{II} .

The active nodes on the master patch and the remaining active nodes on the slave patch are classified as master nodes. The rest are considered as inactive nodes as they do not contribute to the formulation of both b_0 and b_1 .

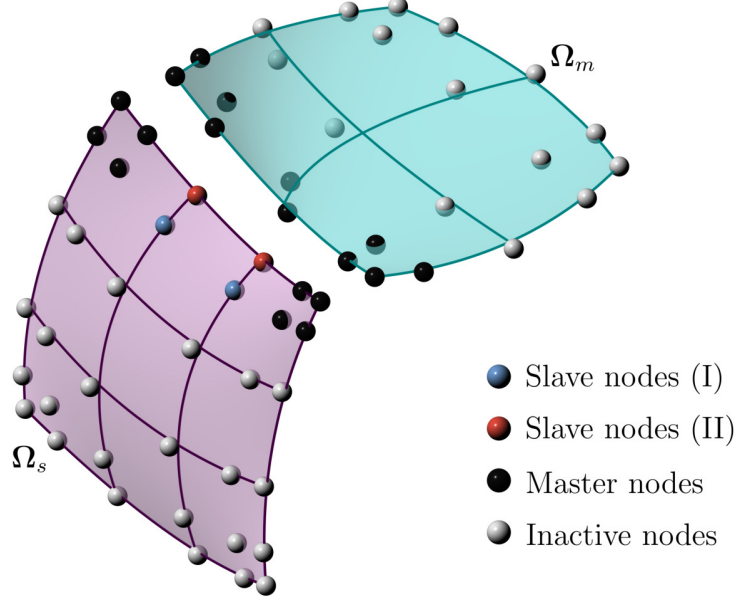


Figure 7: The classification of all basis functions for the two-patch non-conforming Kirchhoff-Love shell in Figure 5. (For interpretation of colors in this figure, readers are referred to the web version of this article.)

We introduce a column-wise permutation matrix \mathbf{P}_c as

$$\begin{bmatrix} \mathbf{I}_1 \\ \mathbf{I}_2 \\ \vdots \\ \mathbf{I}_K \end{bmatrix} = \mathbf{P}_c \begin{bmatrix} \mathbf{I}_s^I \\ \mathbf{I}_s^{II} \\ \mathbf{I}_m \\ \mathbf{I}_{in} \end{bmatrix}, \quad (69)$$

where \mathbf{I}_s^I is the vector form of indices of slave nodes of type I, \mathbf{I}_s^{II} is the vector form of indices of slave nodes of type II, \mathbf{I}_m is the vector form of indices of master nodes and \mathbf{I}_{in} is the vector form of indices of inactive nodes. Then, there exist a row-wise permutation matrix \mathbf{P}_r such that

$$\mathbf{B}_p = [\mathbf{P}_r \otimes \mathbf{I}_{3 \times 3}] \mathbf{B} [\mathbf{P}_c \otimes \mathbf{I}_{3 \times 3}] = \begin{bmatrix} \mathbf{B}_1^1 & \mathbf{B}_1^2 & \mathbf{B}_1^3 & \mathbf{0} \\ \mathbf{0} & \mathbf{B}_2^1 & \mathbf{B}_2^2 & \mathbf{0} \end{bmatrix}, \quad (70)$$

where \otimes is the tensor product operator, $\mathbf{I}_{3 \times 3}$ is the 3×3 identity matrix, \mathbf{B}_1^1 is the contribution of the first type of B-spline basis functions in the discretization of b_1 and \mathbf{B}_2^2 is the contribution of the second type of B-spline basis functions in the discretization of b_0 . Under the row-wise permutation matrix \mathbf{P}_r , \mathbf{B}_1^1 and \mathbf{B}_2^2 become identity submatrices. Under a rank-preserving transformation \mathbf{T} we can eliminate the submatrix \mathbf{B}_1^2 such that

$$\mathbf{T}\mathbf{B}_p = \begin{bmatrix} \mathbf{I} & \begin{bmatrix} \mathbf{B}_1^3 - \mathbf{B}_1^2\mathbf{B}_2^3 \\ \mathbf{B}_2^3 \end{bmatrix} & \mathbf{0} \end{bmatrix}. \quad (71)$$

We may now take

$$\mathbf{B}_p^\perp = \begin{bmatrix} \mathbf{B}_1^2\mathbf{B}_2^3 - \mathbf{B}_1^3 & \mathbf{0} \\ -\mathbf{B}_2^3 & \mathbf{0} \\ \hline \mathbf{I} \end{bmatrix}. \quad (72)$$

The vector basis of the null space of \mathbf{B} can now be obtained from

$$\mathbf{B}^\perp = [\mathbf{P}_c \otimes \mathbf{I}_{3 \times 3}] \mathbf{B}_p^\perp. \quad (73)$$

When the constraint is not homogeneous, i.e. $\mathbf{R} = [\mathbf{0} \quad \mathbf{R}_{p_1}]^T \neq \mathbf{0}$, we have

$$\mathbf{B}\mathbf{U}^{\text{non}} = \mathbf{R} \implies \mathbf{T}\mathbf{B}_p [\mathbf{P}_c \otimes \mathbf{I}_{3 \times 3}]^T \mathbf{U}^{\text{non}} = \mathbf{T}\mathbf{R}_p, \quad (74)$$

where $\mathbf{R}_p = [\mathbf{P}_r \otimes \mathbf{I}_{3 \times 3}] \mathbf{R}$. The transformation matrix \mathbf{T} subtracts the transformation of the C^0 continuity constraint from the rotational constraint and the residual of C^0 continuity constraint is $\mathbf{0}$. Hence, \mathbf{R}_p is invariant under \mathbf{T} . Since $\mathbf{T}\mathbf{B}_p$ takes the form (13), following Equation (16), a particular solution can be explicitly constructed without seeking for the Moore-Penrose inverse as

$$[\mathbf{P}_c \otimes \mathbf{I}_{3 \times 3}]^T \mathbf{U}^{\text{non}} = \begin{bmatrix} \mathbf{R}_p \\ \mathbf{0} \end{bmatrix} \implies \mathbf{U}^{\text{non}} = [\mathbf{P}_c \otimes \mathbf{I}_{3 \times 3}] \begin{bmatrix} \mathbf{R}_p \\ \mathbf{0} \end{bmatrix}. \quad (75)$$

5 Numerical results

In this section, we demonstrate the performance of the proposed Kirchhoff-Love shell coupling formulation through several challenging benchmarks, including both linear and non-linear problems. To validate the accuracy of the proposed formulation, two types of dual bases, i.e., the global dual basis and the enriched Bézier dual basis, are used in all benchmarks. We label the results computed with the i^{th} -order *global* and enriched *Bézier* dual bases by $G-Q_i$ and $B-Q_i$, respectively. Note that the i^{th} -order enriched Bézier dual basis is constructed such that it satisfies the polynomial reproduction property up to degree $i-2$ as it is desirable to guarantee the optimality of the scheme [57].

For fourth order problems with a smooth solution \mathbf{u} , the approximation error of the deformations \mathbf{u}^h in L_2 -norm and H_2 -norm over the entire domain Ω are given by [58]:

$$\|\mathbf{u} - \mathbf{u}^h\|_{L_2(\Omega)} \leq Ch^{\min\{p+1, 2p-2\}}, \quad (76)$$

and

$$\|\mathbf{u} - \mathbf{u}^h\|_{H_2(\Omega)} \leq Ch^{\min\{p-1, 2p-2\}}, \quad (77)$$

where p is the order of basis functions, C is a constant that is independent of the mesh size h . Hence, for basis functions of order 2, 3, 4, the convergence orders are 2, 4, 5 in the L^2 norm and 1, 2, 3 in the H^2 norm, respectively.

5.1 Linear problems

5.1.1 Simply supported plate under sinusoidal load

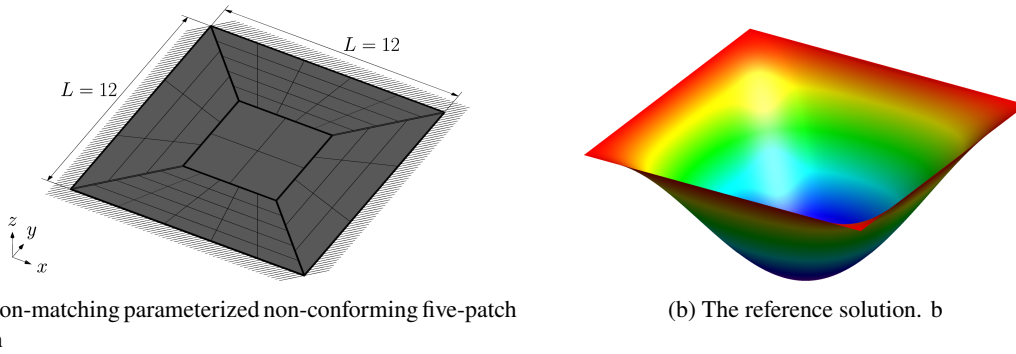


Figure 8: The decomposition and parameterization of the domain $[0, 12] \times [0, 12]$ and the reference solution that satisfies $u = 0$ on $\partial\Omega$.

In the first example, we study a plate of size $L \times L = 12 \times 12$, thickness $t = 0.375$, Young's modulus $E = 4.8 \times 10^5$, Poisson's ratio $\nu = 0.38$ and subjected to a sinusoidal pressure $p(x, y) = \sin(\pi \frac{x}{L}) \sin(\pi \frac{y}{L})$ (in $-z$ direction). The analytical solution of the vertical displacement is given by [59] (see Figure 8)

$$w(x, y) = -\frac{L^4}{4D\pi^4} \sin\left(\frac{\pi x}{L}\right) \sin\left(\frac{\pi y}{L}\right), \quad (78)$$

where $D = \frac{Et^3}{12(1-\nu^2)}$ is the flexural rigidity of the plate. The computational domain is decomposed into five non-conformingly coupled patches as shown in Figure 8. The simply supported boundary condition is applied by setting $\mathbf{u} = 0$ on the boundary.

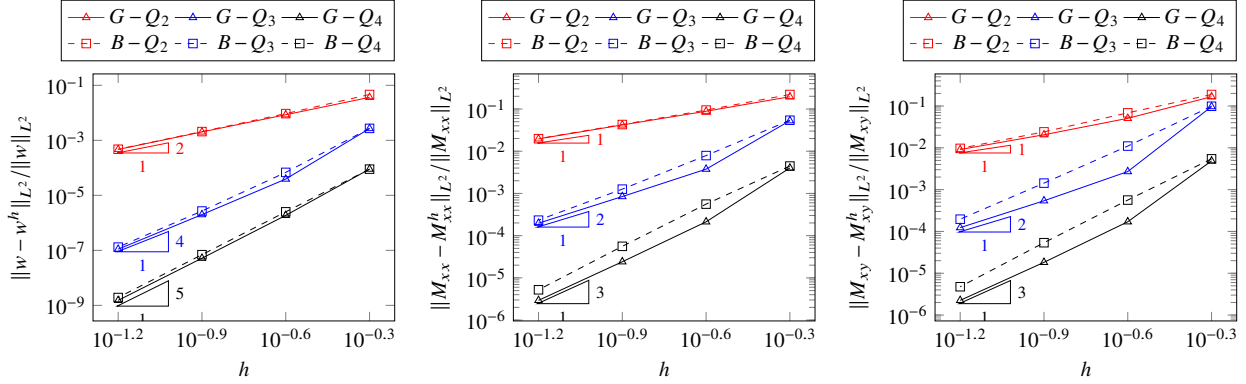


Figure 9: Convergence plots for the simply supported plate under sinusoidal pressure load. Left: error of w measured in L^2 norm. Middle: error of M_{xx} measured in L^2 norm. Right: error of M_{xy} measured in L^2 norm.

Figure 9 shows the convergence of the approximated vertical displacement w^h , bending moment M_{xx}^h and M_{xy}^h to the analytical solution for $p = 2, 3$ and 4 . As expected, both the enriched Bézier dual basis and the global dual basis yield optimal results for all polynomial orders in all three measures. For the displacement error, there is no visible difference between the enriched Bézier dual basis and the global dual basis in all considered polynomial orders. The enriched Bézier dual basis appears to obtain slightly worse bending moment results, but the convergence rates remains optimal.

Contour plots of $\text{err} = u_z^h - u_z$, $\text{err} = M_{xx}^h - M_{xx}$ and $\text{err} = M_{xy}^h - M_{xy}$ for cubic basis are given in Figure 10. As can be seen, the error levels for two types of dual bases are similar with all three error measures. For the enriched Bézier dual basis, due to its locality, error spikes are formed along intersections and highest error spikes are observed at vertices for M_{xx} and M_{xy} . The global dual basis, on the other hand, seems to yield more evenly distributed error inside the patches. This is because the global dual basis has global support, which results in coupling error spreading to the interior.

5.1.2 Scordelis-Lo roof problem

We then consider the Scordelis-Lo roof problem as depicted in Figure. 11a. In this problem, a cylindrical shell roof (Young's modulus $E = 432\text{MPa}$, Poisson's ratio $\nu = 0$, thickness $t = 0.25\text{m}$), under distributed gravity load ($f = 90\text{N/m}^2$), is supported by rigid diaphragms on both curved edges (i.e. $u_x = u_z = 0$). The maximum vertical displacement occurs on the free edge at $\frac{L}{2}$, and a reference solution, $u_z = -0.300592457\text{m}$, is given in [60].

The roof structure is decomposed into four patches which are discretized non-conformingly as shown in Figure. 11a. Figure. 11b demonstrates the effect of the proposed constraint. As can be seen, with only C^0 continuity constraint enforced, although the deformed surface remains continuous all intersections fail to transfer the bending moments from one patch to another. Hence, connections act like hinges, and kinks are formed along all intersections. By enforcing the additional constraint, the smoothness of the roof structure is preserved even though the mesh is non-conformingly discretized.

The sparsity patterns for the stiffness matrices corresponding to the global dual basis and the enriched Bézier dual basis are shown in Figures 12a and b, respectively. As can be seen, the stiffness matrix constructed using the enriched Bézier dual basis is much sparser than that constructed using the global dual basis.

Figure. 13 shows the vertical displacement of the midpoint of the free edge for different polynomial degrees. Converged results are obtained from both the global dual basis and the enriched Bézier dual basis for all polynomial orders and are compared with the result obtained from single NUBRS patch (Q_i). For quartic basis functions, the relative error is reduced to 0.1% with only one refinement for both dual bases. The accuracy of the four-patch configurations is very similar to the single patch one. To better study the performance of the proposed coupling formulation, we compare the displacement field of the four-patch mesh to a reference solution obtained from a very fine single patch mesh as

shown in Figure 14. Optimal convergence rates are attained for all polynomial orders. The convergence plots of the enriched Bézier dual basis is indistinguishable to that of the global dual basis.

5.1.3 Pinched hemispherical shell problem

In this example, we consider a hemispherical shell pinched at the top and subjected to four radial point loads (see Figure. 15a). The bottom circumferential edge of the hemisphere is free. The thickness of the shell is $t = 0.04$ and the material properties are $E = 6.825 \times 10^7$ and $\nu = 0.3$. The hemisphere is initially decomposed into twelve quartic NURBS patches as shown in Figure 15b, the control points and corresponding weights can be found in [61]. Note that the twelve-patch parameterization is degeneracy-free. The radial displacement at the point A is monitored and a reference solution, $u_x = 0.0924$, can be found in [26].

The convergence of the radial displacement at point A is plotted in Figure 16. As can be seen, the enriched Bézier dual basis achieves comparable results with the global dual basis for $p = 4$ but slightly worse results for $p = 5$.

5.1.4 T-beam

Shell structures with kinks and sharp folds are widely used in practice. In this example, we consider a T-beam [39] as shown in Figure 17a, which is modeled by three cubic B-spline patches joined at a common edge. The flange is formed by 14×4 and 16×4 B-spline patches and the web is formed by a 12×4 B-spline patch. All patches have a Young's modulus of $E = 10^7$, a thickness of $t = 0.1$ and a Poisson's ratio of $\nu = 0$. The T-beam is pinned (i.e. $\mathbf{u} = 0$) on one side and deflected under a point load of $F = 10$ at one corner of the flange in the $-z$ direction (see Figure 17a). The deformed configuration is shown in Figure 17b, where a maximum value of the displacement at the bottom tip of the web, i.e., $\max(|\mathbf{u}|) = 0.0589$, is observed, which is coincident with the result given in [39].

Figure 18 shows the relative error of the deformed coupling angle between the web and flange with respect to the initial 90° angle. As can be seen, for both the coarse mesh shown in Figure 17a and a mesh after one uniform refinement, the enriched dual basis achieves very small relative error in the region $y \in [0, 14]$ which is better than the global dual basis. Oscillations are observed at the free end of the intersection for all tested cases. We attribute this phenomenon to the dimension of the discretized Lagrange multiplier spaces. A Lagrange multiplier space with codimension four of the trace space renders all twelve control points at the free end of the intersection as master nodes. Therefore, constraints at this region can not transfer stresses very well from one patch to the other. h -refinement can easily reduce the error magnitude as well as the size of the oscillation region. Owing to the compact supports, the oscillation region of the result from the enriched Bézier dual basis is smaller than the result from the global dual basis for both coarse and fine meshes.

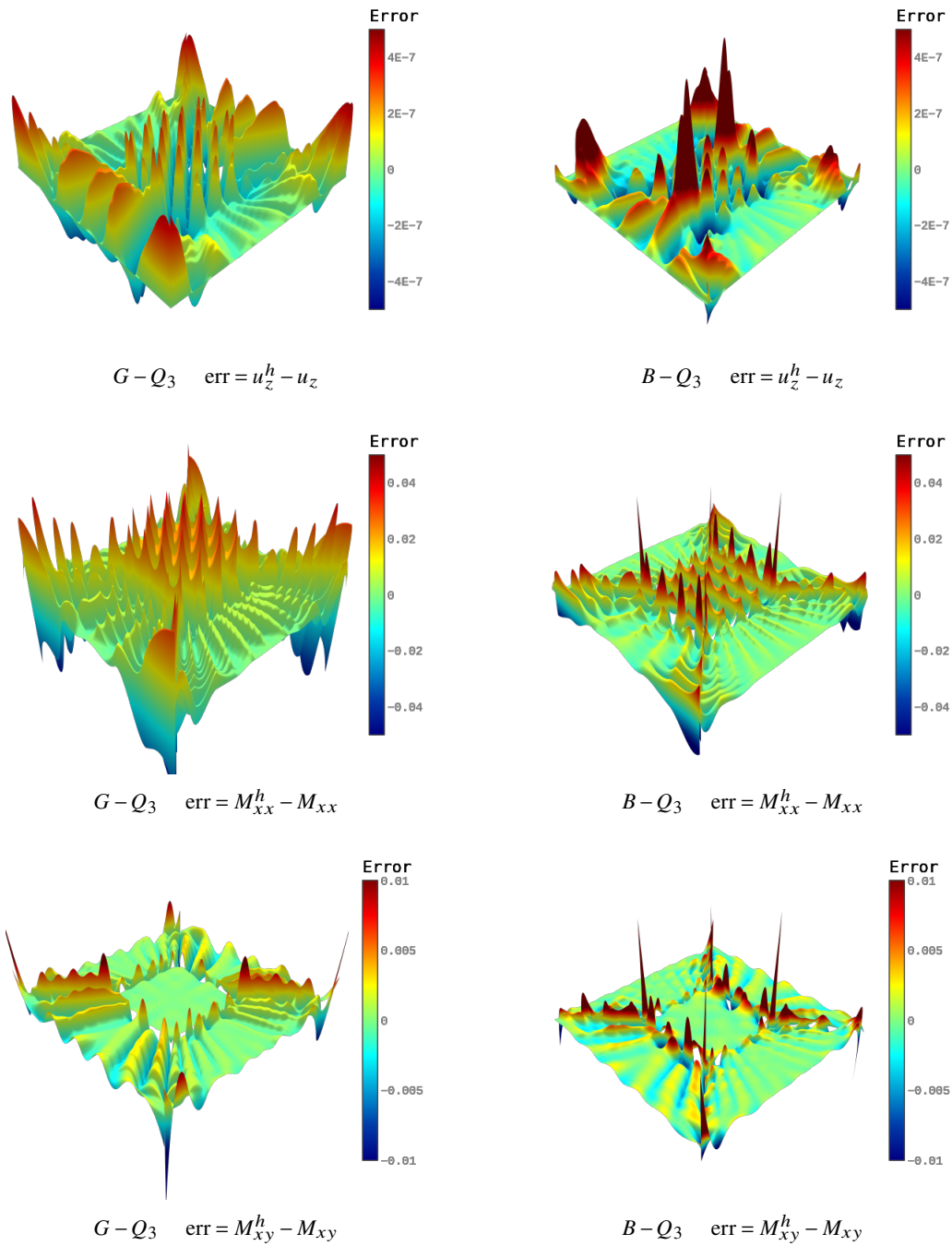


Figure 10: Contour plots of $\text{err} = u_z^h - u_z$, $\text{err} = M_{xx}^h - M_{xx}$ and $\text{err} = M_{xy}^h - M_{xy}$ for the simply supported plate under sinusoidal load ($p = 3$, and the mesh is obtained after one refinement).

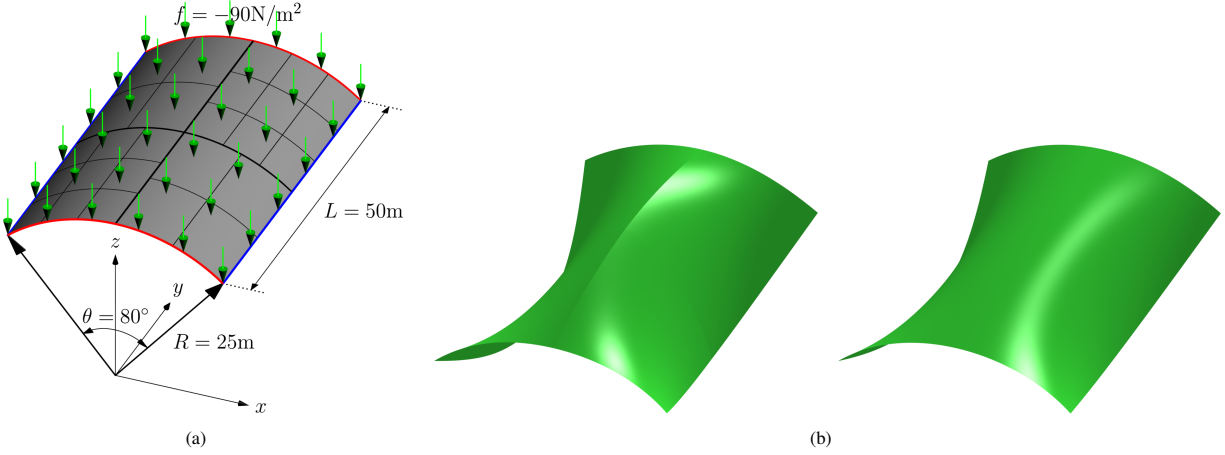


Figure 11: The Scordelis-Lo roof problem: (a) Schematic and parameterization. Note that the blue edges are free, while the red edges are fixed in x and z directions. (b) Deformed Scordelis-Lo roof (scaling factor of 20 is applied to the displacement). Left: Only the C^0 continuity constraint is applied. After deformation, kinks are formed along intersections. Right: The C^1 continuity constraint is also applied. The deformed surface is as smooth as a single patch.

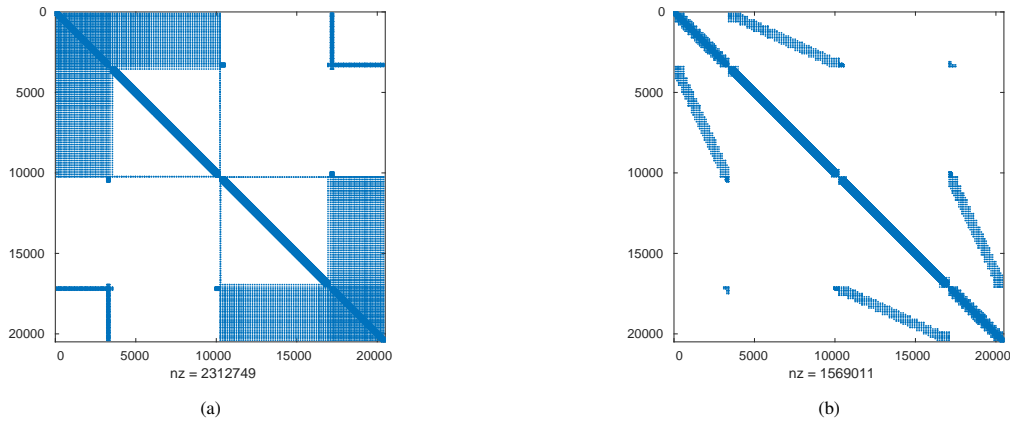


Figure 12: Stiffness matrix sparsity patterns for (a) the coupled linear system using the global dual basis, and (b) the coupled linear system using the enriched Bézier dual basis for the Scordelis-Lo roof problem. The stiffness matrices are computed from the four-patch domain in Figure 11a after 4 levels of refinement.

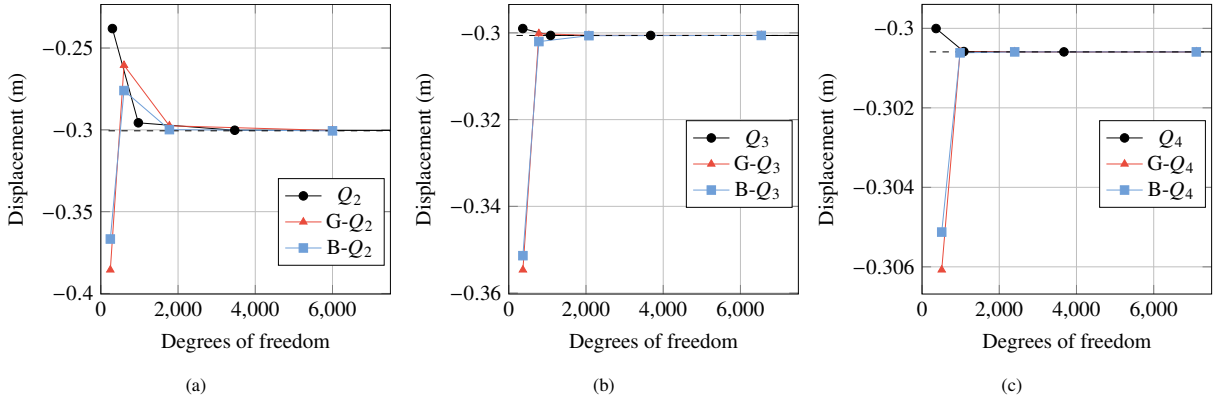


Figure 13: Scordelis-Lo roof problem: a comparison of the vertical displacement at the midpoint of the free edge for different dual basis functions and degrees.

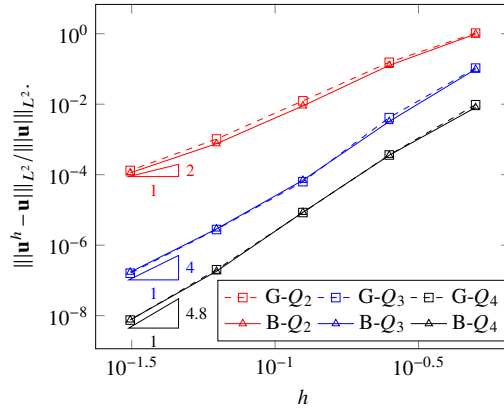


Figure 14: The convergence plot for the Scordelis-Lo roof problem.

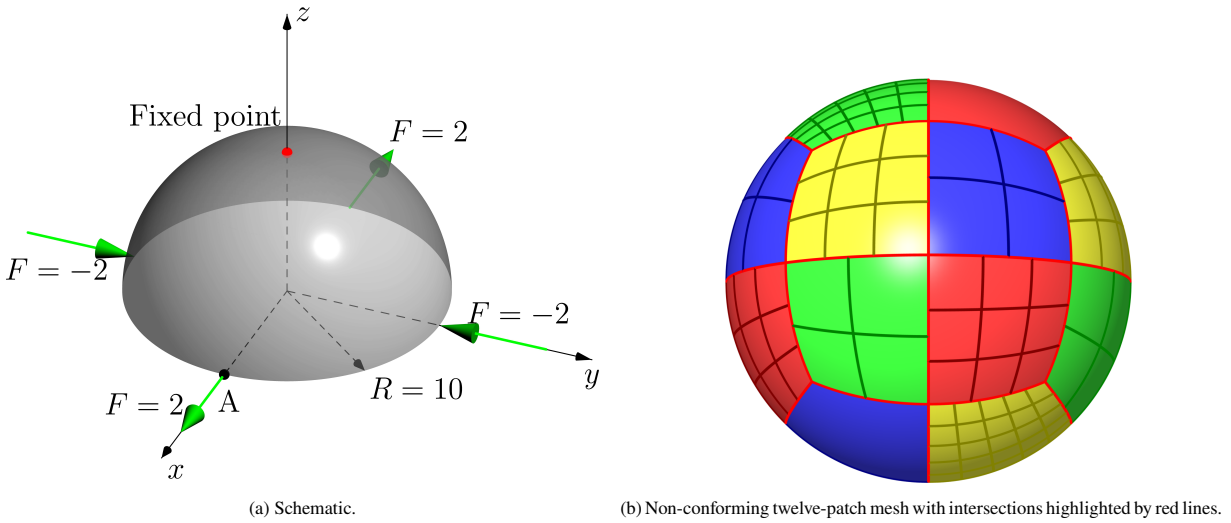


Figure 15: Schematic and mesh setup of the pinched hemisphere shell problem. Rigid body modes are suppressed by fixing the four corner nodes of each patch on the top.

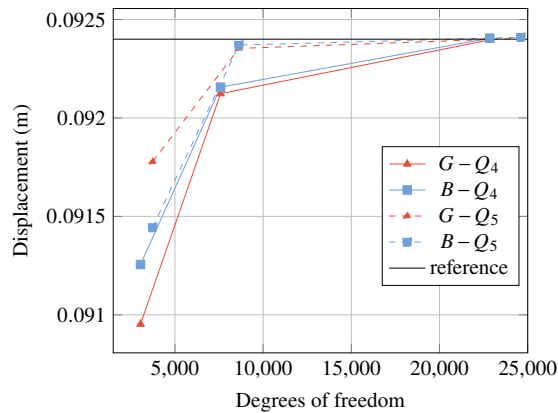


Figure 16: Pinched hemispherical shell problem: a comparison of the radial displacement at point A for different dual basis functions and degrees.

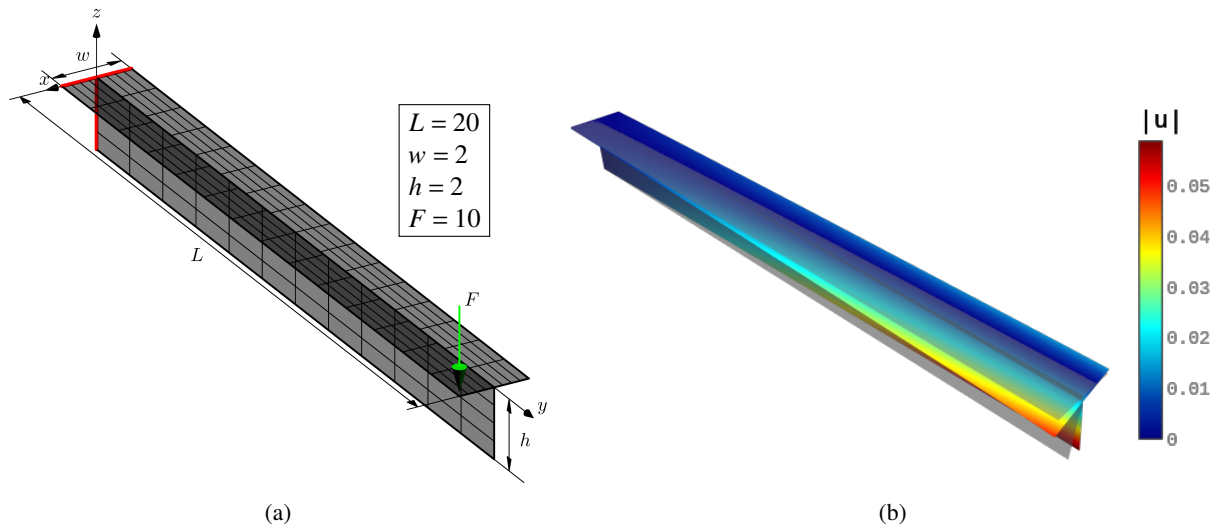


Figure 17: T-beam problem: (a) Schematic and parameterization. Note red edges indicate pinned ends (i.e. $\mathbf{u} = 0$). (b) Deformed configuration with a scale factor of 10.

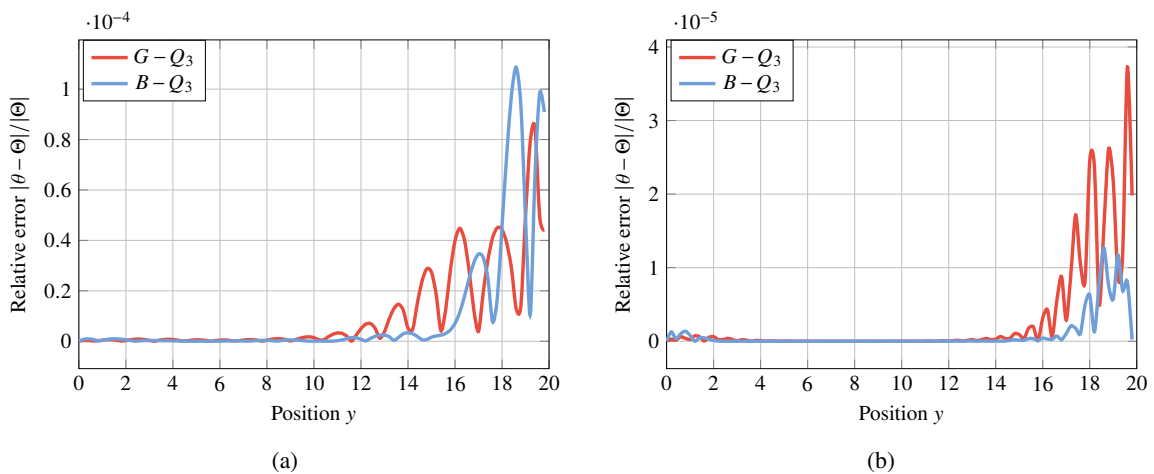


Figure 18: Relative error of angle between the flange and web along the intersection for (a) a coarse mesh shown in Figure 17a, (b) a mesh after one uniform refinement.

5.2 Nonlinear problems

5.2.1 Cantilever shell subjected to an end shear force

The first nonlinear problem to be studied is a cantilever shell subjected to an end shear force (see Figure 19a). The length, width and thickness of the cantilever shell are $L = 10$, $b = 1$ and $t = 0.1$, respectively. This model has Young's modulus $E = 1.2 \times 10^6$ and Poisson's ratio $\nu = 0$. The left boundary is clamped ($\mathbf{u} = \frac{\partial \mathbf{u}}{\partial x} = 0$) while the right boundary is subjected to a uniformly distributed shear force in the z -direction with the maximum load of $f = 4$ and the incremental load of $\Delta f = 0.4$. The geometry is decomposed into three patches, which are discretized by 9×3 , 5×2 and 3×3 B-spline elements, respectively (see Figure 19b). A fine mesh obtained by one uniform refinement of the mesh in Figure 19b is also considered in this study. The deformed cantilever is shown in Figure 19c.

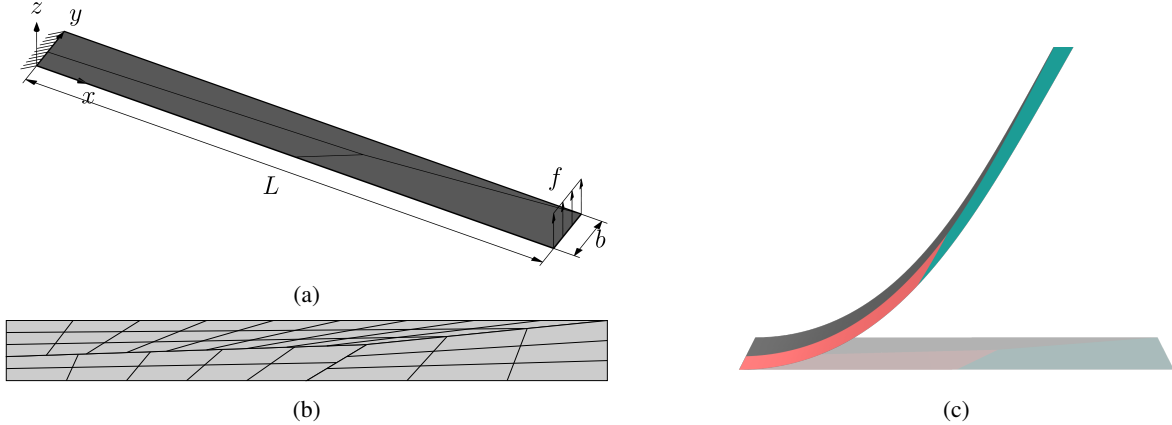


Figure 19: Cantilever shell subjected to an end shear force: (a) Schematic, (b) the three-patch non-matching discretization and (c) the initial and deformed configurations.

Figure 20 shows the shear traction against the horizontal ($-u_x$) and vertical (u_z) displacements at the free end for both the non-conforming multi-patch configuration and the reference results reported by Sze et al. [62]. Due to the heavy distortion of the mesh, the results are as good for quadratic elements with the considered mesh density. However, the results for cubic splines agree with the reference result even for the coarse mesh. For all tested cases, the difference between the results obtained from the enriched Bézier dual basis and the global dual basis are negligible.

5.2.2 Cantilever shell subjected to end moment

In the second example, we study a cantilever shell subjected to an end moment (see Figure 21a). The length, width and thickness of the cantilever are $L = 12$, $b = 1$ and $t = 0.1$, respectively. The material parameters are the same as the previous example. The right boundary is clamped while a bending moment, $M = \frac{2\pi EI}{L}$, is applied at the free end such that the cantilever shell rolls up into a circular arc, where $I = \frac{bt^3}{12}$ is the moment of inertia of the section. The cantilever shell is subdivided into two patches, i.e., the left patch consisting of 10×6 quadratic elements and the right patch consisting of 10×4 quadratic elements (see Figure 21a). A finer mesh is obtained by a uniform refinement of the mesh in Figure 21a. The deformed cantilever shell at different load steps are shown in Figure 21b.

Figure 22 plots load-displacement curves for u_x and u_z components of the free end. As can be seen, similar results have been obtained by the enriched Bézier dual basis and the global dual basis. The results converge to the reference solution [62] as the mesh is refined.

5.2.3 Slit annular plate subjected to a lifting line force

In the following example, we study a slit annular plate subjected to a lifting line force. The problem setup is illustrated in Figure 23a, where the inner radius, outer radius, thickness, maximum vertical traction load and load step are $R_0 = 6$, $R_1 = 10$, $t = 0.03$, $f = 0.8$ and $\Delta f = 0.04$, respectively. Young's modulus is $E = 21 \times 10^6$ and Poisson's ratio is 0. One end of the slit is fully clamped while the other end is lifted under the uniform traction load f . We benchmark the vertical displacements of points A and B. To test the performance of the proposed coupling formulation,

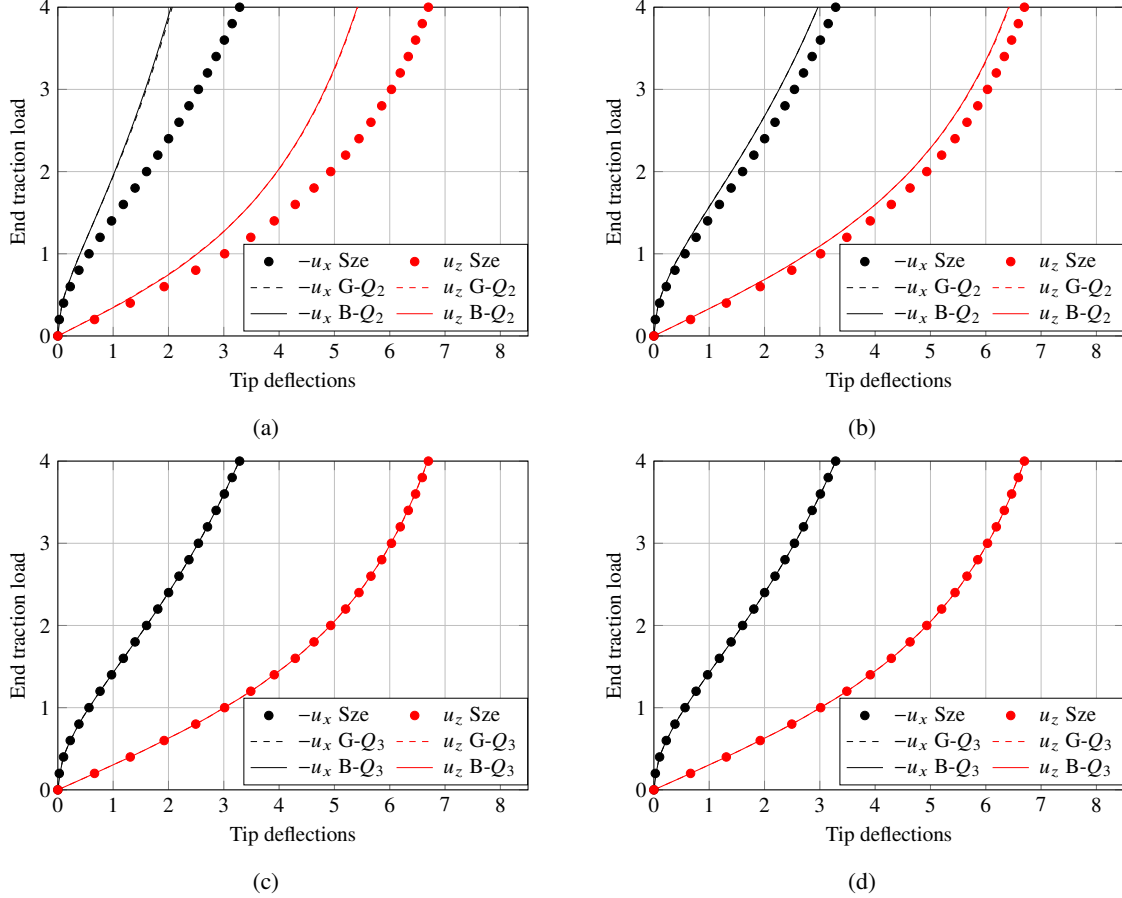


Figure 20: Load-deflection curves for cantilever subjected to an end shear force. The horizontal ($-u_x$) and vertical (u_z) displacements at the free end for (a) a quadratic coarse mesh, (b) a quadratic fine mesh, (c) a cubic coarse mesh and (d) a cubic fine mesh are compared to the results provided in [62].

we decompose the annular plate into three NURBS patches discretized with 6×2 , 6×5 and 6×3 cubic elements, respectively (see Figure 23b). In this example, we also consider a fine mesh obtained by a uniform refinement of the mesh in Figure 23b. The deformed annular plate is shown in Figure 23c.

Figure 24 shows the vertical deflections at points A and B for the non-conforming multi-patch configuration at each load step, where cubic elements are utilized in all considered cases. Even though the multi-patch results obtained from the coarse mesh show slight discrepancies from the reference results provided in [62], they track the reference solutions very well once the mesh is refined. Again, the difference between the results obtained from the enriched Bézier dual basis and the global dual basis are negligible.

5.2.4 Pullout of an open-ended cylindrical shell

In this test, an open-ended cylinder is pulled by a pair of radial forces. The problem setup is illustrated in Figure 25a, where the radius, length, thickness of the cylinder, radial force and load step are $R = 4.953$, $L = 10.35$, $t = 0.094$, $P = 40,000$ and $\Delta P = 1,000$, respectively. The material properties are: Young's modulus $E = 10.5 \times 10^6$ and Poisson's ratio $\nu = 0.3125$. We benchmark u_z at point A, u_x and points B and C, correspondingly. The cylindrical shell is modeled by four NURBS patches, discretized by 32×16 , 28×14 , 28×14 and 32×16 cubic elements, respectively (see Figure 25a). The results given by Sze et al. [62] are used as references. Strong alignments of the computed results with the reference solutions are observed in Figure 26, which demonstrates the accuracy and robustness of the proposed formulation.

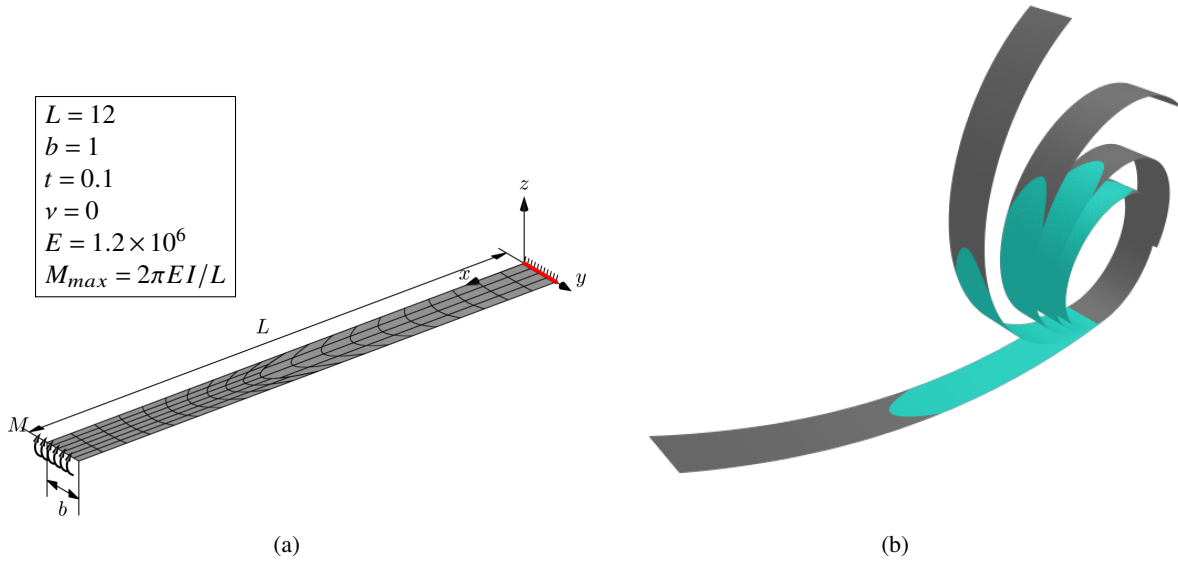


Figure 21: Cantilever shell subjected to end moment: (a) Schematic and parameterization, (b) Deformed configurations. Note that the red line in (a) indicate clamped end, i.e. $\mathbf{u} = \frac{\partial \mathbf{u}}{\partial x} = 0$.

5.2.5 Twisted L-beam

The ability of the proposed formulation to handle kinks in the large deformation configuration is explored with the twisted L-beam problem, as depicted in Figure 27a. The structure is clamped at one end and a point load $F = 30$ is applied to one corner of the opposite end. The thickness of the beam is $t = 0.1$. The Young's modulus is $E = 1.2 \times 10^6$ and the Poisson's ratio is $\nu = 0.3$. The whole L-beam is modeled by two quadratic patches with mismatched parameterizations along the interface as shown in Figure 27a. The angle between two patches varies linearly from the clamped side (90°) to the tip side (60°). The initial and deformed configurations are illustrated in Figure 27b.

A comparison of the vertical deflection at the loaded point between the proposed formulation and a finite element shell solution obtained from Abaqus [63] is shown in Figure 28. The difference between the global dual basis and the enriched Bézier dual basis is negligible. The converged result obtained from Abaqus is 1.5% larger than the proposed approach, which is very small considering the high nonlinearity involved in large deformation and rotation. Figure 29 shows the relative error of the coupling angle along the interface for the mesh in Figure 27a and the mesh after one refinement. The results are similar to the small deformation case (T-beam in Section 5.1.4). After severe deformation, the maximum relative errors are still below 4×10^{-4} for the coarse mesh and below 2×10^{-4} for the fine mesh. Thanks to the compact support of the enriched Bézier dual basis, the oscillation regions obtained by the enriched Bézier dual basis are smaller than those obtained by the global dual basis case for both meshes.

5.2.6 Free form surface with arbitrary curvature and kink

In this example, a free form surface with a curved kink is used to demonstrate the applicability of the proposed method. The free form surface consists of two patches joined with a kink. The angle of the kink varies along the joint. The geometry, discretization and boundary conditions are given in Figure 30a and the contour plot of the displacement in y-direction is given in Figure 30b. The two patches are Gordon-Conns surfaces [64] and the detailed information of the two patches can be found in [65]. The bottom edges (red) are clamped, while the rest edges are free. The upper edge of the left patch is loaded with a traction load $p_y = 10$ in y-direction. Young's modulus is $E = 1.2 \times 10^6$ and Poisson's ratio is $\nu = 0.3$. The thickness is $t = 0.1$.

A comparison of the nonlinear displacement of point A between the proposed formulation and the reference solution $u_y = 0.410789$ given in [65] is shown in Figure 31. The proposed formulations with both the global dual basis and the enriched Bézier dual basis perform very well for all tested degrees.

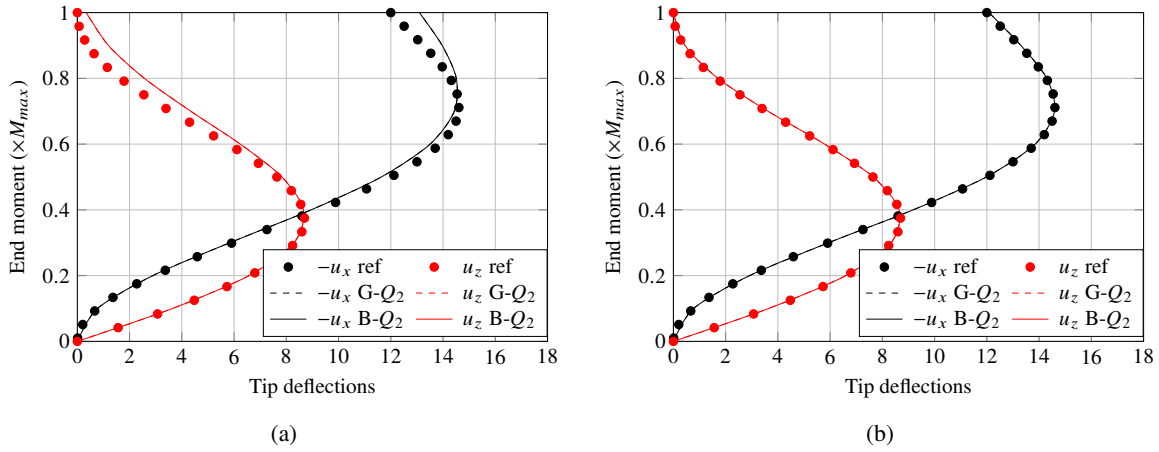


Figure 22: Load-deflection curves for cantilever subjected to an end bending moment. The horizontal ($-u_x$) and vertical (u_z) displacements at the free end for (a) a quadratic coarse mesh (see Figure 21a), (b) a quadratic fine mesh are compared to the analytical result.

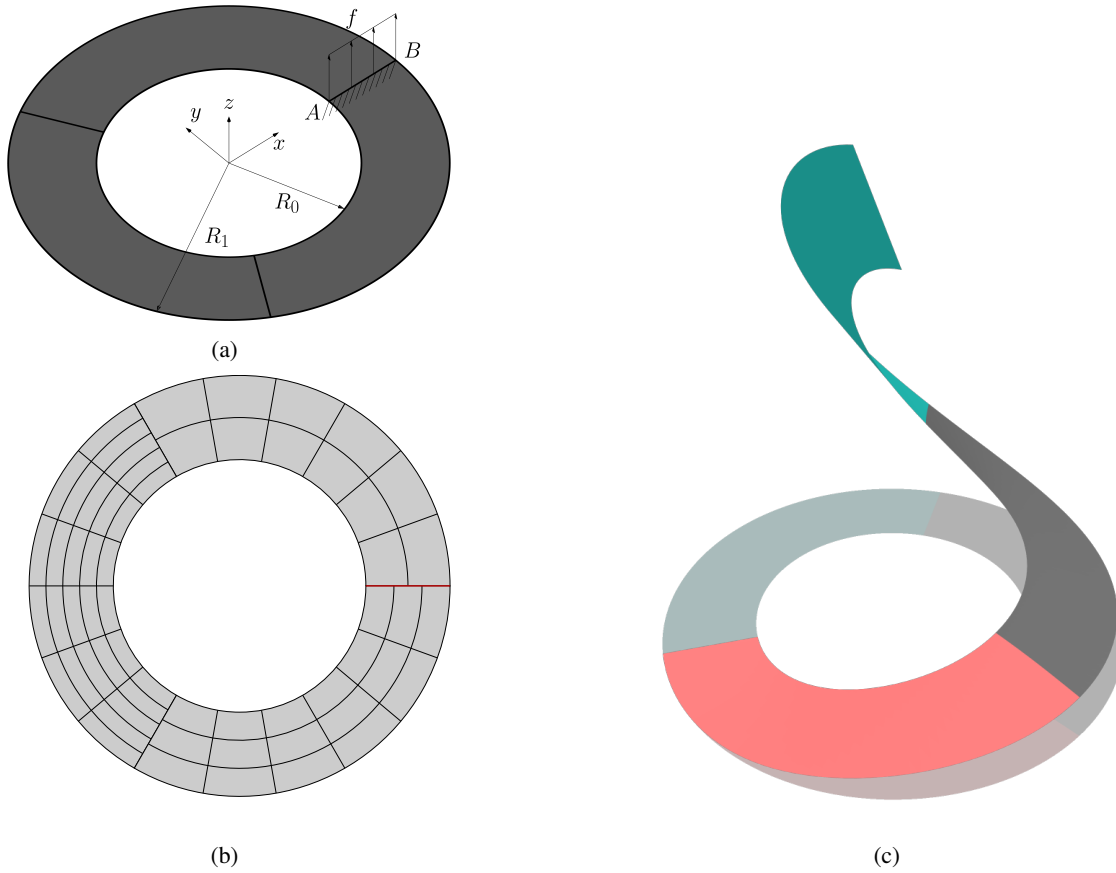
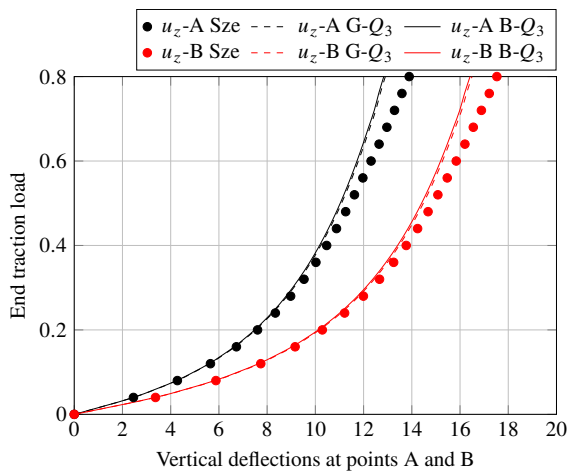
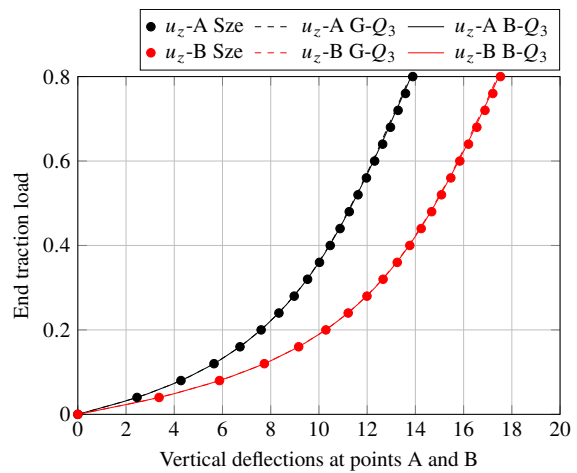


Figure 23: The slit annular plate loaded with the line force f : (a) the problem description, (b) the three-patch non-matching discretization and (c) the initial and deformed configurations.



(a)



(b)

Figure 24: Load-deflection curves for the slit annular plate lifted by a lifting line force. The vertical displacements at tip A and B for (a) a cubic coarse mesh and (b) a cubic fine mesh are compared to the results provided in [62].

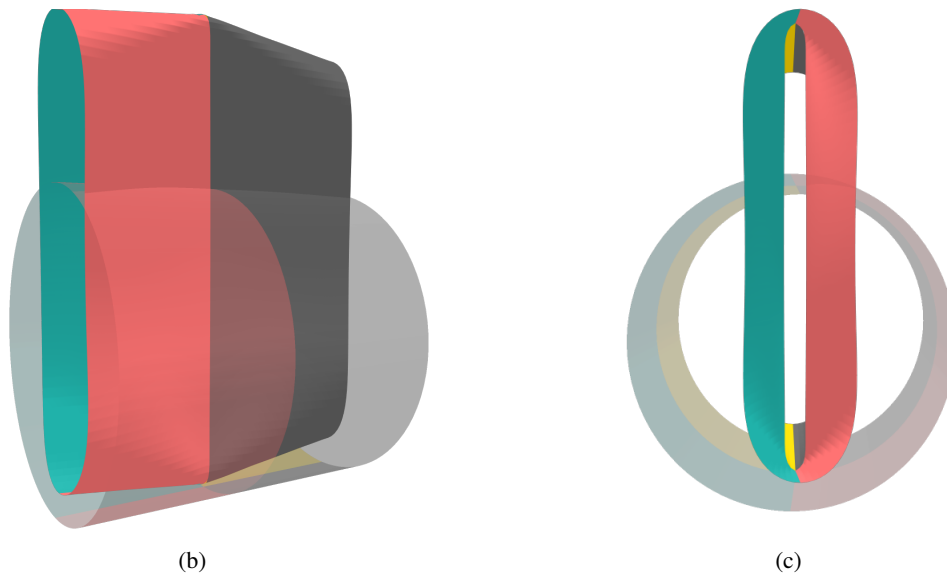
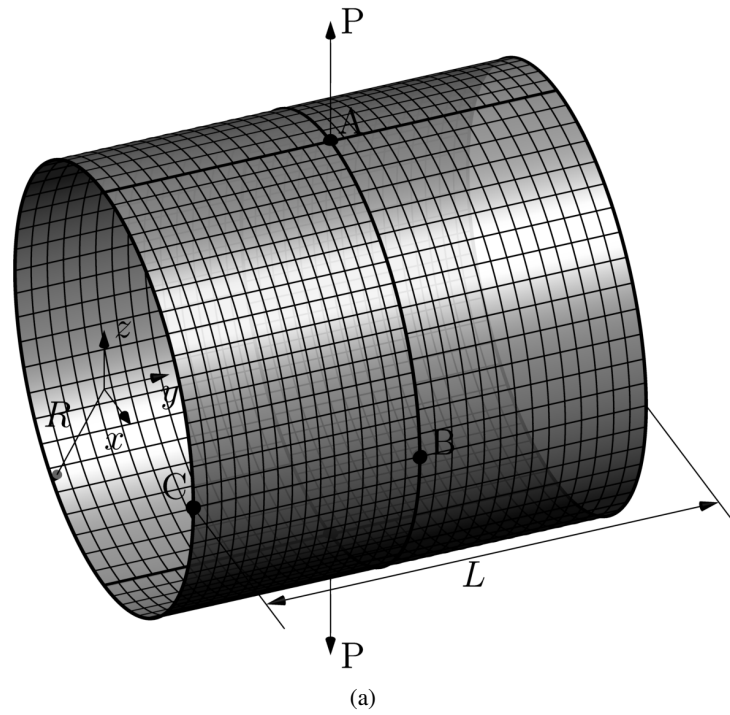


Figure 25: The open-end cylindrical shell subjected to radial pulling forces: (a) the problem description and four-patch non-matching discretization, (b) the initial and deformed configurations in 3D view, and (c) the initial and deformed configurations in y -axis view.

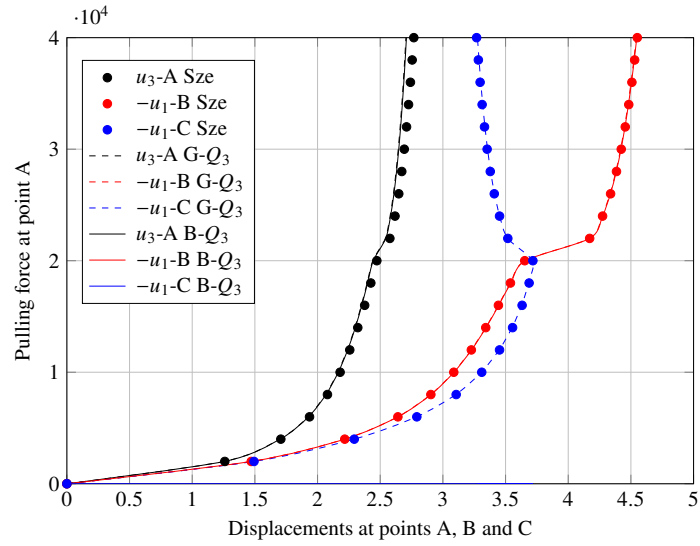


Figure 26: Load-deflection curves of the open-end cylinder subjected to a point pulling load. The results, measured at points A, B and C are compared to the results provided in [62].

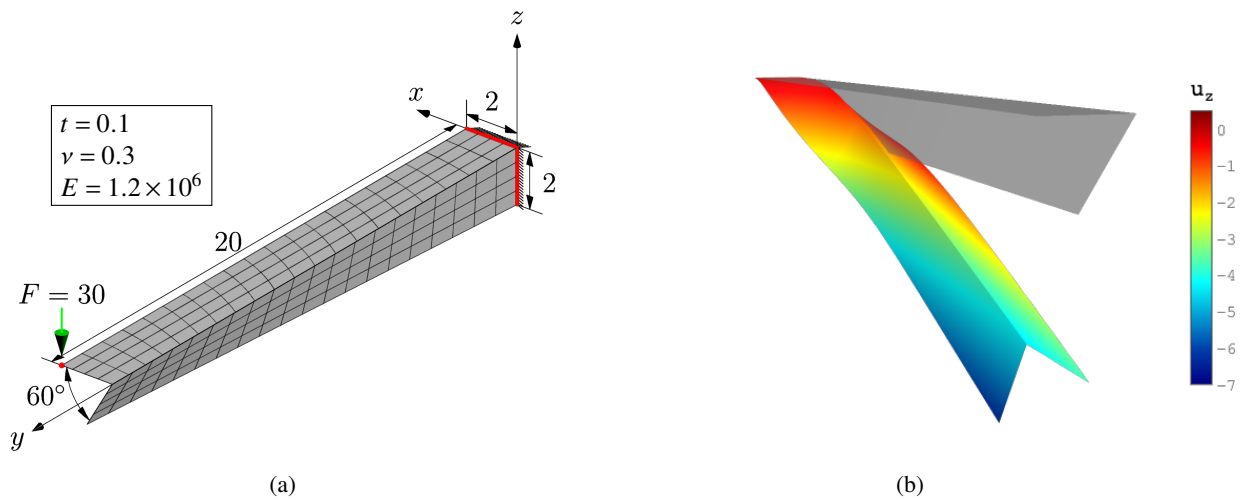


Figure 27: Twisted L-beam problem: (a) Geometry, parameterization and boundary conditions of the problem. Note that red edges are clamped ends (i.e. $\mathbf{u} = \frac{\partial \mathbf{u}}{\partial y} = 0$). (b) Deformed configuration.

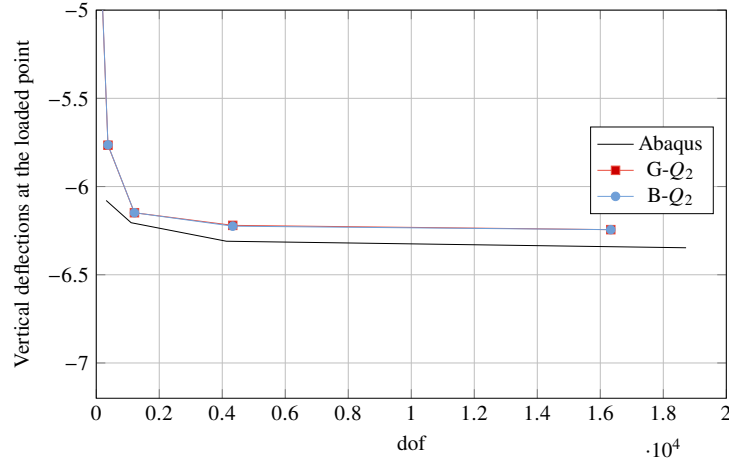


Figure 28: Convergence of the vertical displacement at the loaded point.

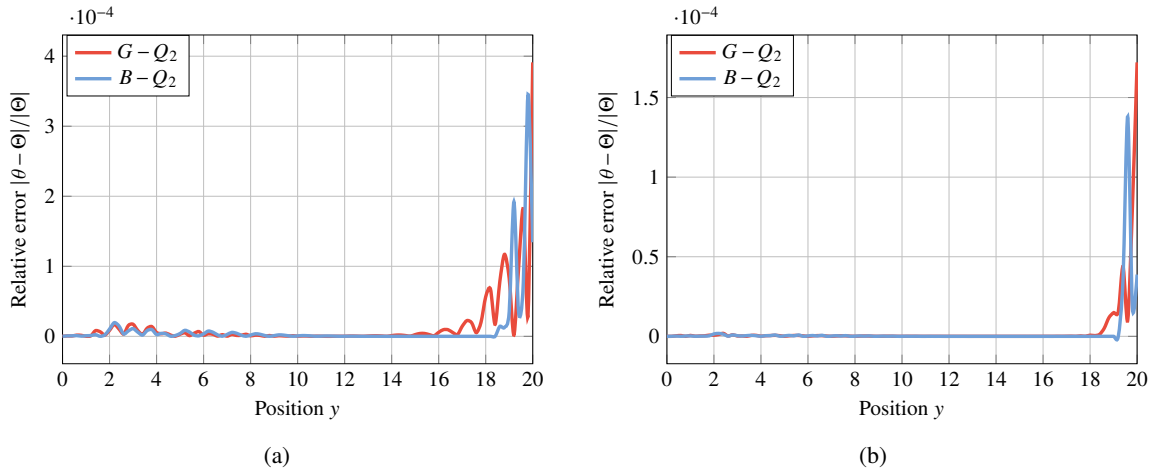


Figure 29: Relative error of angle between two patches along the intersection for (a) a coarse mesh shown in Figure 27a, (b) a fine mesh obtained by uniformly refining the mesh in Figure 27a once.

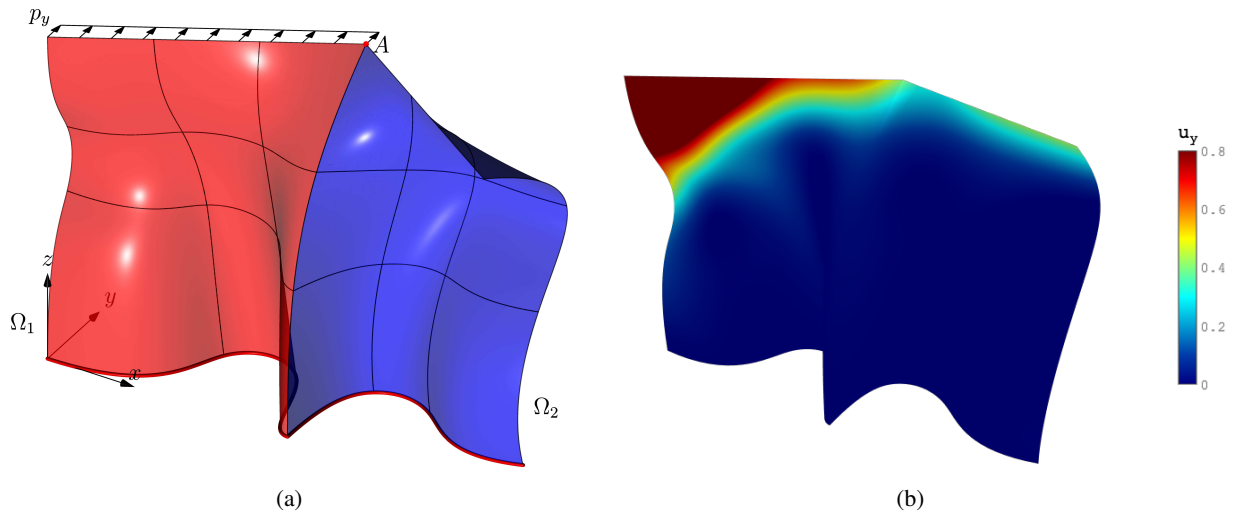


Figure 30: Free form surface with arbitrary curvature and kink: (a) Geometry, parameterization and boundary conditions of the problem. Note that red edges are clamped ends, (b) Deformed configurations.

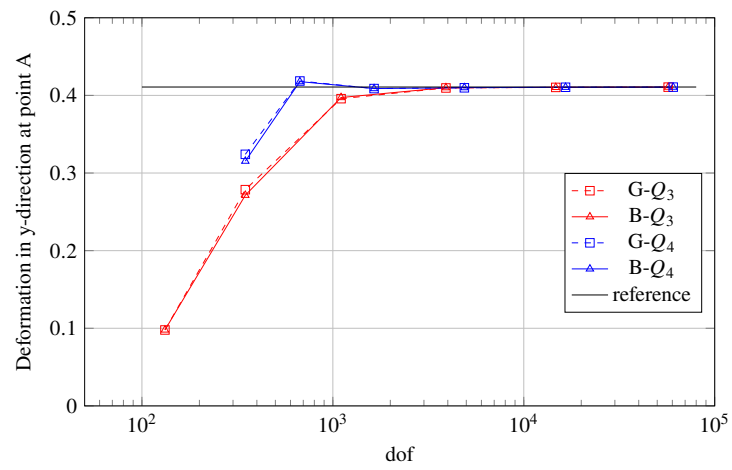


Figure 31: Convergence of the displacement in y-direction at point A.

6 Conclusion

In this paper, we presented a dual mortar formulation for coupling multi-patch Kirchhoff-Love shell problem. The proposed formulation is based on the enriched Bézier dual basis and a dual-compatible constraint. Thanks to the dual-compatible constraint, the biorthogonality between the dual basis functions and the corresponding primal spline basis functions can be extended to the discretized constraint matrix. Hence, the static condensation can be achieved without extra computational effort. As the enriched dual basis functions have local supports, the condensed linear system remains sparse. Additionally, since the dual basis can reproduce polynomials up to a given order, the coupling accuracy is optimal. The constraint formulation utilized in our formulation is generic in the sense that it applies the C^1 continuity when patches meet at interfaces with G^1 -continuity or it preserves the angles when patches meet at kinks. For geometrically nonlinear problems, the constraint becomes nonlinear if a kink appears, which has to be linearized as well. Due to the presence of the residual of the constraint, the linearized constraint is non-homogeneous. Thanks to the unique constraint matrix structure, a particular solution that satisfies the non-homogeneous constraints can be constructed without the need to solve any linear systems which largely simplified the coupling process.

The accuracy and robustness of the proposed formulation are verified by several linear and nonlinear benchmark problems. The Kirchhoff plate and Scordelis-Lo roof problems indicate the optimality of the proposed formulation. The T-beam and L-beam problems demonstrate the ability of the proposed formulation in preserving coupling angles. From the benchmark results, we believe the proposed patch coupling formulation has great potential in addressing complex shell problems in industry.

7 Acknowledgments

The authors acknowledge the support from the U.S. Department of Energy, Office of Science, Office of Advanced Scientific Computing Research, under Award Number DE-SC0017051, and that from the Department of Defense, Navy, Contract: N68335-18-C-0289. We also appreciate the support from Honeywell Federal Manufacturing & Technologies under Contract No. DE-NA0002839 with the U.S. Department of Energy.

The authors would also like to thank Kyle Richardson and Christopher Whetten for polishing the language of this work.

References

- [1] D. Benson, Y. Bazilevs, M.-C. Hsu, T. Hughes, Isogeometric shell analysis: the reissner–mindlin shell, *Computer Methods in Applied Mechanics and Engineering* 199 (5-8) (2010) 276–289.
- [2] F. Brezzi, M. Fortin, R. Stenberg, Error analysis of mixed-interpolated elements for reissner-mindlin plates, *Mathematical Models and Methods in Applied Sciences* 1 (02) (1991) 125–151.
- [3] M. Bischoff, E. Ramm, J. Irlinger, Models and finite elements for thin-walled structures, *Encyclopedia of Computational Mechanics Second Edition* (2018) 1–86.
- [4] J. C. Simo, D. D. Fox, On stress resultant geometrically exact shell model. part i: formulation and optimal parametrization, 1989.
- [5] J. Simo, D. Fox, M. Rifai, On a stress resultant geometrically exact shell model. part ii: The linear theory; computational aspects, *Computer Methods in Applied Mechanics and Engineering* 73 (1) (1989) 53–92.
- [6] J. C. Simo, D. D. Fox, M. S. Rifai, On a stress resultant geometrically exact shell model. part iii: Computational aspects of the nonlinear theory, *Computer Methods in Applied Mechanics and Engineering* 79 (1) (1990) 21–70.
- [7] D. Chapelle, K.-J. Bathe, Fundamental considerations for the finite element analysis of shell structures, *Computers & Structures* 66 (1) (1998) 19–36.
- [8] J. Kiendl, Y. Bazilevs, M. C. Hsu, R. Wüchner, K. U. Bletzinger, The bending strip method for isogeometric analysis of Kirchhoff–Love shell structures comprised of multiple patches, *Computer Methods in Applied Mechanics and Engineering* 199 (37-40) (2010) 2403–2416.
- [9] F. Cirak, M. Ortiz, Fully C1-conforming subdivision elements for finite deformation thin-shell analysis, *International Journal for Numerical Methods in Engineering* 51 (7) (2001) 813–833.
- [10] Z. Zou, T. J. R. Hughes, M. A. Scott, R. A. Sauer, E. J. Savitha, Galerkin formulations of isogeometric shell analysis: Alleviating locking with Greville quadratures and higher-order elements, *Computer Methods in Applied Mechanics and Engineering* 380 (2021) 113757.
- [11] Z. Zou, M. A. Scott, D. Miao, M. Bischoff, B. Oesterle, W. Dornisch, An isogeometric Reissner–Mindlin shell element based on Bézier dual basis functions: Overcoming locking and improved coarse mesh accuracy, *Computer Methods in Applied Mechanics and Engineering* 370 (2020) 113283.
- [12] S. Bieber, B. Oesterle, E. Ramm, M. Bischoff, A variational method to avoid locking—-independent of the discretization scheme, *International Journal for Numerical Methods in Engineering* 114 (8) (2018) 801–827.
- [13] C. Adam, S. Bouabdallah, M. Zarroug, H. Maitournam, Improved numerical integration for locking treatment in isogeometric structural elements. part II: Plates and shells, *Computer Methods in Applied Mechanics and Engineering* 284 (2015) 106–137.
- [14] T. J. R. Hughes, J. A. Cottrell, Y. Bazilevs, Isogeometric analysis: CAD, finite elements, NURBS, exact geometry and mesh refinement, *Computer Methods in Applied Mechanics and Engineering* 194 (39) (2005) 4135–4195.
- [15] J. A. Cottrell, A. Reali, Y. Bazilevs, T. J. Hughes, Isogeometric analysis of structural vibrations, *Computer methods in applied mechanics and engineering* 195 (41-43) (2006) 5257–5296.
- [16] M. J. Borden, C. V. Verhoosel, M. A. Scott, T. J. R. Hughes, C. M. Landis, A phase-field description of dynamic brittle fracture, *Computer Methods in Applied Mechanics and Engineering* 217 (2012) 77–95.
- [17] M. J. Borden, T. J. R. Hughes, C. M. Landis, C. V. Verhoosel, A higher-order phase-field model for brittle fracture: Formulation and analysis within the isogeometric analysis framework, *Computer Methods in Applied Mechanics and Engineering* 273 (2014) 100–118.
- [18] X. Qian, Full analytical sensitivities in NURBS based isogeometric shape optimization, *Computer Methods in Applied Mechanics and Engineering* 199 (29) (2010) 2059–2071.

- [19] W. A. Wall, M. A. Frenzel, C. Cyron, Isogeometric structural shape optimization, *Computer Methods in Applied Mechanics and Engineering* 197 (33) (2008) 2976–2988.
- [20] A. Buffa, G. Sangalli, R. Vázquez, Isogeometric analysis in electromagnetics: B-splines approximation, *Computer Methods in Applied Mechanics and Engineering* 199 (17) (2010) 1143–1152.
- [21] A. Buffa, G. Sangalli, R. Vázquez, Isogeometric methods for computational electromagnetics: B-spline and T-spline discretizations, *Journal of Computational Physics* 257 (2014) 1291–1320.
- [22] Y. Bazilevs, V. M. Calo, Y. Zhang, T. J. R. Hughes, Isogeometric Fluid–structure Interaction Analysis with Applications to Arterial Blood Flow, *Computational Mechanics* 38 (4) (2006) 310–322.
- [23] Y. Bazilevs, M. C. Hsu, M. A. Scott, Isogeometric fluid–structure interaction analysis with emphasis on non-matching discretizations, and with application to wind turbines, *Computer Methods in Applied Mechanics and Engineering* 249 (2012) 28–41.
- [24] L. Piegl, W. Tiller, *The NURBS Book*, 2nd Edition, Springer, Berlin ; New York, 1996.
- [25] T. Sederberg, J. Zheng, A. Bakenov, A. Nasri, T-splines and T-NURCCs, in: *ACM SIGGRAPH 2003 Papers, SIGGRAPH '03*, ACM, New York, NY, USA, 2003, pp. 477–484.
- [26] J. Kiendl, K. U. Bletzinger, J. Linhard, R. Wüchner, Isogeometric shell analysis with Kirchhoff–Love elements, *Computer Methods in Applied Mechanics and Engineering* 198 (49-52) (2009) 3902–3914.
- [27] D. Benson, S. Hartmann, Y. Bazilevs, M.-C. Hsu, T. Hughes, Blended isogeometric shells, *Computer Methods in Applied Mechanics and Engineering* 255 (2013) 133–146.
- [28] D. J. Benson, Y. Bazilevs, M.-C. Hsu, T. J. R. Hughes, A large deformation, rotation-free, isogeometric shell, *Computer Methods in Applied Mechanics and Engineering* 200 (13-16) (2011) 1367–1378.
- [29] W. Dornisch, R. Müller, S. Klinkel, An efficient and robust rotational formulation for isogeometric Reissner–Mindlin shell elements, *Computer Methods in Applied Mechanics and Engineering* 303 (2016) 1–34.
- [30] S. Hosseini, J. J. Remmers, C. V. Verhoosel, R. De Borst, An isogeometric solid-like shell element for nonlinear analysis, *International Journal for Numerical Methods in Engineering* 95 (3) (2013) 238–256.
- [31] R. Bouclier, T. Elguedj, A. Combescure, On the development of nurbs-based isogeometric solid shell elements: 2d problems and preliminary extension to 3d, *Computational Mechanics* 52 (5) (2013) 1085–1112.
- [32] T. X. Duong, F. Roohbakhshan, R. A. Sauer, A new rotation-free isogeometric thin shell formulation and a corresponding continuity constraint for patch boundaries, *Computer Methods in Applied Mechanics and Engineering* 316 (2017) 43–83.
- [33] W. Dornisch, S. Klinkel, Treatment of reissner–mindlin shells with kinks without the need for drilling rotation stabilization in an isogeometric framework, *Computer Methods in Applied Mechanics and Engineering* 276 (2014) 35–66.
- [34] A. Goyal, B. Simeon, On penalty-free formulations for multipatch isogeometric kirchhoff–love shells, *Mathematics and Computers in Simulation* 136 (2017) 78–103.
- [35] D. Miao, Z. Zou, M. A. Scott, M. J. Borden, D. C. Thomas, Isogeometric bézier dual mortaring: The enriched bézier dual basis with application to second-and fourth-order problems, *Computer Methods in Applied Mechanics and Engineering* 363 (2020) 112900.
- [36] Z. Zou, M. A. Scott, M. J. Borden, D. C. Thomas, W. Dornisch, E. Brivadis, Isogeometric Bézier dual mortaring: Refineable higher-order spline dual bases and weakly continuous geometry, *Computer Methods in Applied Mechanics and Engineering* 333 (2018) 497–534.
- [37] Z. Zou, *Isogeometric shell analysis: Multi-patch coupling and overcoming locking*, Ph.D. thesis, Brigham Young University, Provo (2020).

- [38] P. Oswald, B. Wohlmuth, On polynomial reproduction of dual FE bases, in: Thirteenth international conference on domain decomposition methods, 2001, pp. 85–96.
- [39] A. J. Herrema, E. L. Johnson, D. Proserpio, M. C. Wu, J. Kiendl, M.-C. Hsu, Penalty coupling of non-matching isogeometric kirchhoff–love shell patches with application to composite wind turbine blades, *Computer Methods in Applied Mechanics and Engineering* 346 (2019) 810–840.
- [40] M. Breitenberger, A. Apostolatos, B. Philipp, R. Wüchner, K.-U. Bletzinger, Analysis in computer aided design: Nonlinear isogeometric b-rep analysis of shell structures, *Computer Methods in Applied Mechanics and Engineering* 284 (2015) 401–457.
- [41] A. Apostolatos, M. Breitenberger, R. Wüchner, K.-U. Bletzinger, Domain decomposition methods and Kirchhoff-Love shell multipatch coupling in isogeometric analysis, in: *Isogeometric Analysis and Applications 2014*, Springer, 2015, pp. 73–101.
- [42] T. Hirschler, R. Bouclier, A. Duval, T. Elguedj, J. Morlier, The embedded isogeometric kirchhoff–love shell: From design to shape optimization of non-conforming stiffened multipatch structures, *Computer Methods in Applied Mechanics and Engineering* 349 (2019) 774 – 797.
- [43] S. Schuß, M. Dittmann, B. Wohlmuth, S. Klinkel, C. Hesch, Multi-patch isogeometric analysis for Kirchhoff–Love shell elements, *Computer Methods in Applied Mechanics and Engineering* 349 (2019) 91–116.
- [44] Y. Guo, Z. Zou, M. Ruess, Isogeometric multi-patch analyses for mixed thin shells in the framework of non-linear elasticity, *Computer Methods in Applied Mechanics and Engineering* 380 (2021) 113771.
- [45] Y. Guo, M. Ruess, Nitsche’s method for a coupling of isogeometric thin shells and blended shell structures, *Computer Methods in Applied Mechanics and Engineering* 284 (2015) 881–905.
- [46] N. Nguyen-Thanh, K. Zhou, X. Zhuang, P. Areias, H. Nguyen-Xuan, Y. Bazilevs, T. Rabczuk, Isogeometric analysis of large-deformation thin shells using rht-splines for multiple-patch coupling, *Computer Methods in Applied Mechanics and Engineering* 316 (2017) 1157–1178.
- [47] F. Cirak, M. Ortiz, P. Schröder, Subdivision surfaces: a new paradigm for thin-shell finite-element analysis, *International Journal for Numerical Methods in Engineering* 47 (12) (2000) 2039–2072.
- [48] A. Wawrzinek, K. Hildebrandt, K. Polthier, Koiter’s thin shells on catmull-clark limit surfaces., in: *VMV*, 2011, pp. 113–120.
- [49] N. Liu, A. E. Jeffers, A geometrically exact isogeometric kirchhoff plate: Feature-preserving automatic meshing and c 1 rational triangular bézier spline discretizations, *International Journal for Numerical Methods in Engineering* 115 (3) (2018) 395–409.
- [50] M. Zareh, X. Qian, Kirchhoff–love shell formulation based on triangular isogeometric analysis, *Computer Methods in Applied Mechanics and Engineering* 347 (2019) 853–873.
- [51] M. Ainsworth, Essential boundary conditions and multi-point constraints in finite element analysis, *Computer Methods in Applied Mechanics and Engineering* 190 (48) (2001) 6323–6339.
- [52] D. Chapelle, K.-J. Bathe, *The finite element analysis of shells-Fundamentals*, Springer Science & Business Media, 2010.
- [53] O. Rodrigues, Des lois géométriques qui régissent les déplacements d’un système solide dans l’espace: et de la variation des cordonnées provenant de ces déplacements considérés indépendamment des causes qui peuvent les produire, 1840.
- [54] L. Coox, F. Greco, O. Atak, D. Vandepitte, W. Desmet, A robust patch coupling method for NURBS-based isogeometric analysis of non-conforming multipatch surfaces, *Computer Methods in Applied Mechanics and Engineering* 316 (2017) 235–260.
- [55] E. Brivadis, A. Buffa, B. Wohlmuth, L. Wunderlich, Isogeometric mortar methods, *Computer Methods in Applied Mechanics and Engineering* 284 (2015) 292–319.

- [56] L. Wunderlich, A. Seitz, M. D. Alaydin, B. Wohlmuth, A. Popp, Biorthogonal splines for optimal weak patch-coupling in isogeometric analysis with applications to finite deformation elasticity, *Computer Methods in Applied Mechanics and Engineering* 346 (2019) 197–215.
- [57] D. Miao, Isogeometric bezier dual mortaring and applications.
- [58] A. Tagliabue, L. Dede, A. Quarteroni, Isogeometric analysis and error estimates for high order partial differential equations in fluid dynamics, *Computers & Fluids* 102 (2014) 277–303.
- [59] S. P. Timoshenko, S. Woinowsky-Krieger, *Theory of plates and shells*, McGraw-hill, 1959.
- [60] L. Coox, F. Maurin, F. Greco, E. Deckers, D. Vandepitte, W. Desmet, A flexible approach for coupling nurbs patches in rotationless isogeometric analysis of kirchhoff–love shells, *Computer Methods in Applied Mechanics and Engineering* 325 (2017) 505–531.
- [61] S. Dedoncker, L. Coox, F. Maurin, F. Greco, W. Desmet, Bézier tilings of the sphere and their applications in benchmarking multipatch isogeometric methods, *Computer Methods in Applied Mechanics and Engineering* 332 (2018) 255–279.
- [62] K. Sze, X. Liu, S. Lo, Popular benchmark problems for geometric nonlinear analysis of shells, *Finite elements in analysis and design* 40 (11) (2004) 1551–1569.
- [63] D. Hibbit, B. Karlsson, P. Sorensen, *Abaqus/standard analysis user’s manual*, Hibbit, Karlsson, Sorensen Inc, Providence, USA.
- [64] S. A. Coons, *Surfaces for computer-aided design of space forms*, Tech. rep., USA (1967).
- [65] W. Dornisch, J. Stöckler, R. Müller, Dual and approximate dual basis functions for B-splines and NURBS–Comparison and application for an efficient coupling of patches with the isogeometric mortar method, *Computer Methods in Applied Mechanics and Engineering* 316 (2017) 449–496.